The Thesis Committee for Yunjun Wu
Certifies that this is the approved version of the following thesis :

A Vorticity Based Model and its Application to Flow around an Impulsively Started Cylinder

APPROVED BY

SUPERVISING COMMITTEE:

George Biros, Supervisor

Spyros A. Kinnas, Co-Supervisor

A Vorticity Based Model and its Application to Flow around an Impulsively Started Cylinder

by

Yunjun Wu, B.S.

THESIS

Presented to the Faculty of the Graduate School of

The University of Texas at Austin

in Partial Fulfillment

of the Requirements

for the Degree of

MASTER OF SCIENCE IN ENGINEERING

THE UNIVERSITY OF TEXAS AT AUSTIN

May 2016

Acknowledgments

First of all I'd like to thank my supervisors, Professor Kinnas and Professor Biros, for being patient to guide me during my master's study at University of Texas at Austin. I sincerely appreciate Professor Kinnas from Ocean Engineering Group, who inspired and encouraged me during the last two semesters, dedicating time and efforts to my thesis. I'd also like to thank Professor Biros from ICES, who guided me in the early stage of my study and gave me invaluable suggestions on my works.

I would also like to thank Dr. Tian for his early works. Without his works and help, I wouldn't be able to start this thesis work. Although it was a tough process, I learned a lot from Dr. Tian's works and codes and it is my honor to continue his work in Ocean Engineering Group.

Many thanks to Mr. Chunlin Wu who helped me and collaborated with me in this subject. I am also grateful to Mr. Yiran Su, Mr. Guangyao Wang, Mr. Weikang Du, Mr. Zhihao Li and Mr. Seungnam Kim who share their opinions on my thesis. I enjoyed the time with all the members in OEG.

I'd also like to say thanks to Dr. Ben-Yakar from Mechanical Engineering, who kindly gave guidance on my Teaching Assistant job during my 2 years at Austin. I'd miss the time in the ME130L lab with the students and all the other TAs.

I appreciate the support and love from my parents and Uncle Wei. Thanks for the support from Yu and Bowser. Thanks to my fellows at ANSYS, Inc and Professor Ding Hang.

A Vorticity Based Model and its Application to Flow around an Impulsively Started Cylinder

Yunjun Wu, M.S.E.
The University of Texas at Austin, 2016

Supervisors: George Biros
Spyros A. Kinnas

An improved model of VIScous Vorticity Equation (VISVE) in 2-D is proposed and implemented in this thesis. Based on the original model, non-orthogonal terms have been included in this model in order to apply to meshes with skewness. A surface pressure model has been designed in order to predict the time evolution of pressure and force. Parallelization has been implemented in the code to shorten the computational time cost.

The proposed method is applied to an impulsive started cylinder, which is a classic unsteady separated flow in 2-D. New griding has been created in order to apply to the cylinder geometry. Results are correlated with published experimental and numerical data. The flow patterns were captured in the converging solution. Grid independence and sufficiency of the computational domain are evaluated.

Table of Contents

List of Tables

List of Figures

Chapter 1

Introduction

1.1 Background

Accurately predicting the performance of propellers has being a challenge in ocean engineering. As panel methods and various models widely accepted by the community, problems arise as these models fail to predict the thrust and torque at high loading.

Separating from the leading edge at high angle of attack could be crucial to the pressure prediction on the blade. The vortex sheet generated from the leading edge connect to the trailing edge is difficult to simulate using the panel methods.

A vortex model was therefore developed based on viscous theory, using a panel method to enforce the boundary condition locally. The vortex transport equation in the whole fluid field can help us determine complex flow separation. Considering that the vorticity concentrates in a small range of the flow field, this viscous vortex model is spacially compact and numerically efficient. Enforcing the non-slip boundary condition on the wall surface, a panel method is used in the vortex sheet along the boundary, as a local correction to the viscous model.

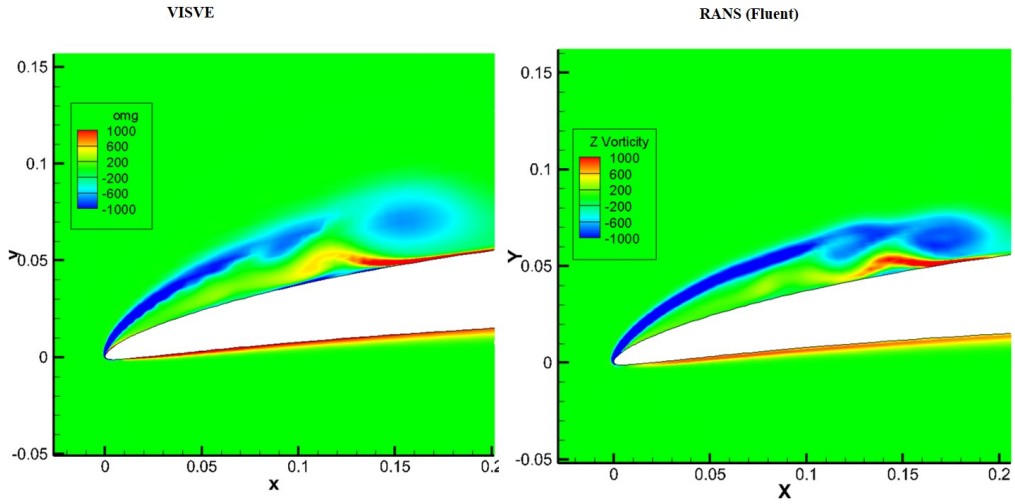

Figure 1.1: Tian (2014) VISVE result of a 2D hydrofoil with $AOA = 10°$ comparing with Navier-Stokes model result [26].

1.2 Motivation

A 3D vorticity based method, named VIScous Vortex Equation (VISVE), was developed by Tian (2014) [26], but has not been fully validated.

In Tian's work [26] [27], the VISVE results of a hydrofoil were presented and compared with a Navier-Stokes solver result. In Figure1.1, the two results are comparable, while the discrepancy is not negligible in the flow field. Both of the results shows the start up leading edge vortex (LEV) moving downstream with the flow. It can be observed that VISVE result has more diffusion effect in the terms of vorticity transportation. Due to that diffusion, the intensity of the vortex predicted by VISVE is smaller than that from the Navier-Stokes solver results.

Additionally, a pressure model as introduced in Tian's work. However,

this pressure model is not well validated by comparing to other published data.

Therefore, a precise validation and improvement is necessary at this point for the VISVE model. A model needs to be established and details of the results need to be compared with published data. Various previous articles and papers studied cylinder flow and provided both numerical and experimental results. Impulsively started cylinder flow is a classic, yet challenging, unsteady separation flow problem, but also a practical application for the current VISVE model.

1.3 Objective

The objective of this research is to improve the current 2D VISVE model and validate it using an impulsively started cylinder flow.

The original objective of the VISVE model of Tian's work [26] [27] was to predict the leading edge vortex of a hydrofoil and then propeller blade. Validation of the VISVE 3D as applied to hydrofoils was recently presented by Wu (2016) [31].

According to the new geometry, the griding and the solver need to be modified so that it can be applied to a more general flow field. The calculation domain needs to be efficient while covers all the regions where the vorticities concentrate. New griding scheme should be available for a more general geometry such like that for a cylinder flow. Most of the grids should be distributed close to the solid surface, where the vorticity generated. We also require suf-

ficient number of cells in the wake region where the vortex shedding patterns are developed.

A more general VISVE solver is crucial to this research work, since the original 2D model can only deal with orthogonal or nearly orthogonal mesh. A new pressure model should also be developed, instead of evaluating the pressure throughout the flow field. Surface pressure should be evaluated along the solid boundary.

Long time calculation provide more insight on the classical von Karman vortex street. The periodic vortex shedding is a crucial feature not only for impulsive started cylinder, but also for the design of risers used in the offshore industry as well as for anti-singing propeller blade sections.

1.4 Overview

This thesis is organized into six main chapters:

Chapter 2 reviews the existing vortex methods including the existing VISVE code. It also provide a close look in the current studies in impulsively started cylinder flow.

Chapter 3 presents the VISVE method in 2D flow, including the solver improvement in the accommodation for non-orthogonal mesh and also a new model of surface pressure.

Chapter 4 provides the details of the application of cylinder flow, introducing the grids and parallel computing of VISVE.

Chapter 5 presents the results and discussion of the impulsively started flow. The results from VISVE are compared with experimental data and other numerical simulations. The effect of grid resolution and the computational efficiency are also addressed in this chapter.

Chapter 6 summarizes the conclusions of the thesis, and provides some recommendations for future work.

Chapter 2

Literature Review

This chapter reviews the literature on two topics: numerical vortex methods and experimental and computational studies of flow around impulsively started cylinder.

2.1 Vortex Methods

Discrete vortex methods are widely used by the researchers to predict the 2D separate flow. Katz (1981) [11] used a discrete vortex method to analyze the separated unsteady inviscid flow around a cambered airfoil. A 2D foil under high angle of attack was simulated using vortex lattice approach and the periodic shedding vortex and forces were predicted in Katz's work. Spalart and Leonard (1981) [25] developed a vortex tracking model, in which large value of Reynolds number was assumed. This work was followed by an improvement in the research of Koumoutsakos and Leonard (1995) [14] in which the model was improved and applied to an impulsively started cylinder flow. The simulation was conducted under wide range of Reynolds number ($40 < Re < 9500$) and closely agreed with experimental data.

Different works were carried on in the separated flow around bluff bodies

using discrete vortex methods. Clements (1973) [6] and Sarpkaya (1975) [24] investigated the vortex shedding patterns under inviscid assumption. However, as discrete vortex methods are well developed in 2D flows, they are still challenging in extending to 3-D flows.

Boundary Element Method (BEM), or panel method, has been applied to analyze the unsteady flow around propellers, first introduced to solve 2D flow around hydrofoils by Giesing (1968) [8]. Kerwin et al (1987) [12] analyzed 2D hydrofoil and ducted propellers confronted by uniform flow using panel method. They simulated steady potential flow of a duct, hub and propeller. This paper was followed by improvement in correction of the trailing edge Kutta condition in Kinnas and Hsin (1994) [13]. Kinnas and Hsin re-evaluated the 2D hydrofoil simulation and included a local error correction to improve the performance of the model.

Instead of solving the Navier-Stokes equations, the viscous vorticity equation is solved using appropriate mesh and by employing a finite difference method or a finite volume method. In Wu et al's work (1995) [32] a divergence free velocity-vorticity formulation in 3D was developed and a lid-driven flow simulation was conducted to test the model. Hansen et al (2003)[10] applied a finite difference vortex method in a cylindrical coordinate to predict axisymmetric flow in pipes.

The VISVE was developed by Tian (2014) [26] solving the viscous vorticity equation in both 2D and 3D flow field applying the BEM at the solid boundary in order to satisfied the non-slip boundary condition. Through this

model, the inviscid model BEM could be applied to predict flow field of a viscous flow. Tian's model captures the essential flow features such as leading edge vortex and tip vortex and the results are comparable to the RANS solution.

2.2 Impulsively Stared Cylinder Flow

Behind a 2D cylinder, before the 3D effect occurs, two regime of laminar vortex were discovered: at small Reynolds number ($Re < 49$)the wake comprises a steady re-circulation region of two symmetrically placed vortices on each side of the wake. When the Reynolds number goes beyond that, the re-circulation region develops into instabilities. The vortex oscillations are periodic in the wake. The two regimes are well studied in the past fifty years as summarized by Williamson (1996) [29].

Among various studies on cylinder flow, the impulsively started cylinder problem is studied as a prototype of unsteady separated flows. The Magnus effect was first observed by Prandlt (1925) [21]. Intensive experimental investigations on this subject are presented in Bouard and Coutanceau (1980) [4]. In this experiment a specially designed system were used to produce nearly instantaneous starts. Photos of the streamlines of the flow field were analyzed. The wake evolution process as well as two important flow structure of rapid vortex and forwake, i.e. α and β-phenomena at different Reynolds numbers were observed. However the drag force and pressure measurements were not presented.

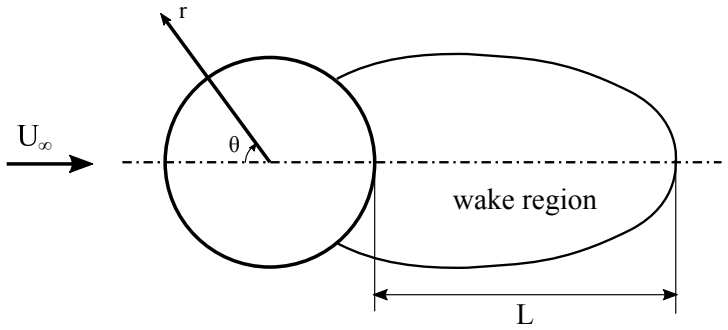

Figure 2.1: Flow geometry of a cylinder flow. $\mathbf{U}_\infty$ is the incoming flow velocity. In polar system, r is the radial direction and θ is the angular direction. L denotes the wake length, which is the distance between the stagnation point in the wake and the tailing edge.

Numerical studies were conducted attempting to generate high-order simulation of the time evolution of this separated flow. Impulsively started flows present a challenge especially in the application of boundary condition and of the initial condition. High-order resolution is required in the numerical simulation, to resolve accurately the separation process.

A viscous vortex method with finite difference method was realized in Chang and Chern's work (1991) [5], in which vortex on the surface were calculated in order to satisfy the boundary condition. They evaluated the surface pressure and the time evolution of the drag force. An adaptive numerical Lagrangian vortex method was employed by Koumoutsakos and Leonard (1995) [14], in which time evolution results of higher resolution were presented. Both of the articles captured the α and β-phenomena that was first observed by Bouard and Coutanceau's experiment [4].

This well studied topic has been applied to various numerical models in order to validate and test the efficiency of the numerical methods. In Qian and Vezza's work (2001) [22], the vorticity transport equation is solved by using the cell-centered finite-volume method and both the early stage development and long term evolution of the impulsively started flow were achieved by their method. High efficiency was achieved by an adaptive fast summation algorithm. Lattice Boltzmann method were also applied to study this subject by Niu et al (2003) [19] and Dupuis et al (2008) [7], including a immersed boundary model in the Lattice Boltzmann method. The results in a case with curved boundary was validated and results with higher resolution were presented.

Besides the static cylinder in impulsively started flow, various topics such as rotating and oscillating cylinder were discussed. Flow over a rotating cylinder was studied by Badr and Dennis (1985) [2] as well as Mittal and Kumar (2003) [17]. Oscillating cylinder was presented in the works of Williamson and Roshko (1988)[30], Guilmineau and Queutey (2002) [9]. These are also challenging topics in numerical simulation.

Chapter 3

Improved Model of VISVE

The 2-D Viscous Vorticity Equation (VISVE) method combining with BEM at boundary was developed by Tian, and was originally only applicable to nearly orthogonal mesh. See more details in Tian (2014) [26].

3.1 Viscous Vorticity Method

Viscous vorticity methods have been used to model separated flows in previous research [14] [22] [10].

The vorticity equation can be derived from the governing equation for an incompressible viscid flow. The Navier-Stokes equations can be written as:

$$\frac{\partial \mathbf{q}}{\partial t} + (\mathbf{q} \cdot \nabla)\,\mathbf{q} = -\frac{\nabla p}{\rho} + \nu \nabla^2 \mathbf{q}, \tag{3.1}$$

in which $\mathbf{q}$ denotes the velocity vector, p and ρ represent the pressure and density, respectively, and ν is the viscosity. By simply taking the curl of equation 3.1, we get vorticity equation

$$\frac{\partial \boldsymbol{\omega}}{\partial t} + (\mathbf{q} \cdot \nabla)\,\boldsymbol{\omega} = (\boldsymbol{\omega} \cdot \nabla)\,\mathbf{q} + \nu \nabla^2 \boldsymbol{\omega}, \tag{3.2}$$

in which $\boldsymbol{\omega}$ denotes the vorticity vector, defined as the curl of the velocity vector $\mathbf{q}$. This is a general vorticity equation which applies to 3D space with

vorticity $\boldsymbol{\omega}$ being a vector. $\frac{\partial \boldsymbol{\omega}}{\partial t}$ denotes the time derivative of vorticity and $(\mathbf{q} \cdot \nabla)\,\boldsymbol{\omega}$ is the convective term. The diffusivity of the vorticity is represented by the term $\nu \nabla^2 \boldsymbol{\omega}$, while $(\boldsymbol{\omega} \cdot \nabla)\,\mathbf{q}$ is the vortex stretching term.

In 2D problems, the vortex stretching term vanishes. The vorticity vector ends up with non-zero value in only one direction, perpendicular to the flow velocities. Thus, $\boldsymbol{\omega}$ is simplified as a scalar:

$$\frac{\partial \omega}{\partial t} + (\mathbf{q} \cdot \nabla)\,\omega = \nu \nabla^2 \omega. \tag{3.3}$$

3.2 Finite Volume Method

In order to develop a Finite Volume Method for our governing equation, we re-write equation 3.3 in conservation form

$$\frac{\partial \omega}{\partial t} + (\mathbf{q} \cdot \nabla)\,\omega = \nabla \cdot (\nu \nabla \omega)\,. \tag{3.4}$$

Integrate equation 3.4 over a certain control volume V, i.e. a grid cell's volume,

$$\int_V \frac{\partial \omega}{\partial t} \mathrm{d}V + \int_V (\mathbf{q} \cdot \nabla)\,\omega \mathrm{d}V = \int_V \nabla\,(\nu \nabla \omega)\,\mathrm{d}V. \tag{3.5}$$

One can apply Gauss divergence theorem to equation 3.5, transforming the volume integral into surface integral,

$$\int_V \frac{\partial \omega}{\partial t} \mathrm{d}V + \int_S \mathbf{q} \omega \mathrm{d}S = \int_S (\nu \nabla \omega) \cdot \mathbf{n} \mathrm{d}S, \tag{3.6}$$

in which S is the control surface, $\mathbf{n}$ is the unit normal vector that pointing outside of the control surface S. If we discretize the surface S into a summation of several faces which are numbered as 1, 2, ..., N, we can discretize the

integration as:

$$\int_V \frac{\partial \omega}{\partial t} \mathrm{d}V + \sum_{j=1}^{N} \left(\mathbf{q}\omega A\right)_j = \sum_{j=1}^{N} \left(\nu \frac{\partial \omega}{\partial n_j} A\right)_j, \tag{3.7}$$

in which, subscript j denoted the values that evaluated on the face j. $\frac{\partial \omega}{\partial n_j}$ is the normal derivative of vorticity calculated on the face j. If we represent the face j 's area of a 2D grid cell as Δl_j, and discretize the time steps as time at n and $n+1$ we get

$$\frac{\omega_{n+1} - \omega_n}{\Delta t} + \sum_{j=1}^{N} \left(\mathbf{q}_j \omega_j \Delta l_j\right) = \sum_{j=1}^{N} \left(\nu \frac{\partial \omega}{\partial n_j} \Delta l_j\right). \tag{3.8}$$

In equation 3.8, the convective term $\mathbf{q}_j \omega_j \Delta l_j$ can be calculated,once we know the velocity and vorticity on the face j. The diffusive term $\nu \frac{\partial \omega}{\partial n_j} \Delta l_j$ is detailed in the next section.

3.3 Diffusive Term in Unstructured Mesh

In structured mesh or orthogonal mesh, the diffusive term can be calculated easily since the derivatives can be calculated in the same direction of the face in x-y coordinates:

$$\nu \frac{\partial \omega}{\partial n} \Delta l_f = \nu \frac{\partial \omega}{\partial x} \Delta l_y = \nu \frac{\omega_1 - \omega_0}{\Delta x} \Delta l_y, \tag{3.9}$$

in which, n denotes the direction from centroid of cell 0 to centroid of cell 1. Δl_y is the distance between the two centroids, which is as same as the difference between the y coordinates of the location. However in non-orthogonal mesh

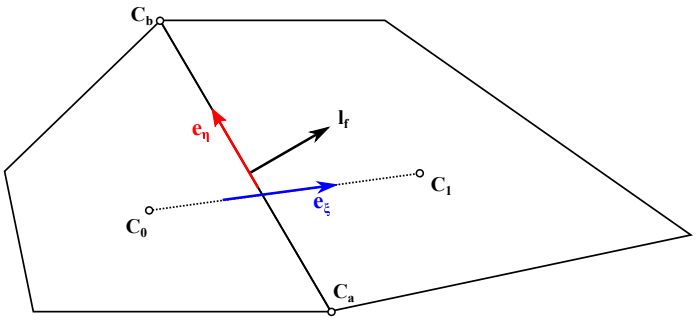

Figure 3.1: Non-orthogonal mesh. C_0 and C_1 are the cell centroids. C_a and C_b are the grid points. l_f is the face vector of face f between the two cells. $\boldsymbol{e}_\xi$ is unit vectors pointing from C_0 to C_1. $\boldsymbol{e}_\eta$ is unit vector pointing from C_a to C_b.

[18], this term should be derived differently as:

$$\nu \frac{\partial \omega}{\partial n_f} \Delta l_f = -\nu \frac{\boldsymbol{l}_f \cdot \boldsymbol{l}_f}{\boldsymbol{l}_f \cdot \boldsymbol{e}_\xi} \left(\omega_\xi\right)_f + \nu \frac{\boldsymbol{l}_f \cdot \boldsymbol{l}_f}{\boldsymbol{l}_f \cdot \boldsymbol{e}_\xi} \boldsymbol{e}_\xi \cdot \boldsymbol{e}_\eta \left(\omega_\eta\right)_f , \tag{3.10}$$

in which $\frac{\partial \omega}{\partial n}$ can no longer be written as $\frac{\omega_1 - \omega_0}{\Delta x}$ as n is not in the direction of x or y coordinates anymore. Face vector $\boldsymbol{l}_f$ has the direction perpendicular to the face, pointing from cell 0 to cell 1, while its magnitude equals to the face area l_f. Unit vector $\boldsymbol{e}_\xi$ points from centroid of cell 0 to 1 as unit vector $\boldsymbol{e}_\eta$ from grid point a to b, as shown in figure 3.1. The derivations can be calculated by

$$\left(\omega_\xi\right)_f = \frac{\omega_1 - \omega_0}{\Delta \xi} \tag{3.11}$$

$$\left(\omega_\eta\right)_f = \frac{\omega_b - \omega_a}{\Delta \eta}. \tag{3.12}$$

In equation 3.10, the first term with $\left(\omega_\xi\right)_f$ is called primary term, while the second term involving with $\left(\omega_\eta\right)_f$ is called secondary term. In orthogonal

mesh, the secondary term equals to zero. Additionally, equation 3.10 can be simplified to equation 3.9 in orthogonal mesh.

The vorticity values are stored at cell centroids, providing a convenience way to calculate primary deviation $(\omega_\xi)_f$. However, to calculate secondary deviation $(\omega_\eta)_f$, we will need to know the values at the grid points C_a and C_b in order to calculate $\frac{\omega_b - \omega_a}{\Delta\eta}$. Surely we can use interpolations to approach that. When it comes to 3D problems, it is not easy to define direction η [18]. Thus, gradient is introduced in equation 3.13 to calculate the secondary term instead of using values on the grid points.

$$\nu \frac{\partial \omega}{\partial n_j} \Delta l_f = -\nu \frac{\boldsymbol{l}_f \cdot \boldsymbol{l}_f}{\boldsymbol{l}_f \cdot \boldsymbol{e}_\xi} (\omega_\xi)_f + \nu \nabla\omega \cdot \boldsymbol{l}_f - \nu \frac{\boldsymbol{l}_f \cdot \boldsymbol{l}_f}{\boldsymbol{l}_f \cdot \boldsymbol{e}_\xi} \nabla\omega \cdot \boldsymbol{e}_\xi \tag{3.13}$$

3.4 Calculation of Gradient

Using least squares method [18], the gradient is calculated using solutions of the neighbor cells. Assuming a linear profile of a quantity ϕ that is store at the cell centroids, as shown in Figure 3.4. If ϕ is stored at a neighboring cell numbered as j near the center cell numbered as 0, then the value of ϕ can be written as:

$$\phi_0 + \nabla\phi_0 \cdot \Delta\mathbf{r_j} = \phi_j, \tag{3.14}$$

where $\nabla\phi_0$ is the gradient at cell 0, $\Delta\mathbf{r_j}$ denotes the vector from centroid of cell C_0 to centroid of cell C_j. Unfolding the dot product, we write:

$$\Delta x_j \left.\frac{\partial \phi}{\partial x}\right|_0 + \Delta y_j \left.\frac{\partial \phi}{\partial y}\right|_0 = \phi_j - \phi_0 \tag{3.15}$$

This equation can apply to all the neighboring cells around cell C_0. For convenience, it can be rewritten as:

$$\mathbf{Md} = \Delta\phi, \tag{3.16}$$

where $\mathbf{M}$ is a $J \times 2$ matrix

$$\mathbf{M} = \begin{bmatrix} \Delta x_1 & \Delta y_1 \\ \Delta x_2 & \Delta y_2 \\ \vdots & \vdots \\ \Delta x_j & \Delta y_j \end{bmatrix}, \tag{3.17}$$

$\mathbf{d}$ is a vector of gradient that we a after for

$$\mathbf{d} = \begin{bmatrix} \frac{\partial\phi}{\partial x}|_0 \\ \frac{\partial\phi}{\partial y}|_0 \end{bmatrix}, \tag{3.18}$$

and $\mathbf{\Delta}\phi$ denotes the vector of differences of ϕ

$$\mathbf{\Delta}\phi = \begin{bmatrix} \phi_1 - \phi_0 \\ \phi_2 - \phi_0 \\ \vdots \\ \phi_j - \phi_0 \end{bmatrix}. \tag{3.19}$$

Equation 3.16 represents j equations for all of the j neighbor cells around cell C_0, with only 2 unknowns, components of gradient vector, in j equations. When $j > 2$, this is an over-determined system, meaning that the solution of $\mathbf{d}$ can not satisfy all the equations in equation 3.16. The best possible solution we could obtain is the one that gives the smallest RMS of the difference between the cells. In other words, the error

$$R_j = \Delta x_j \frac{\partial\phi}{\partial x}\bigg|_0 + \Delta y_j \frac{\partial\phi}{\partial y}\bigg|_0 - (\phi_j - \phi_0) \tag{3.20}$$

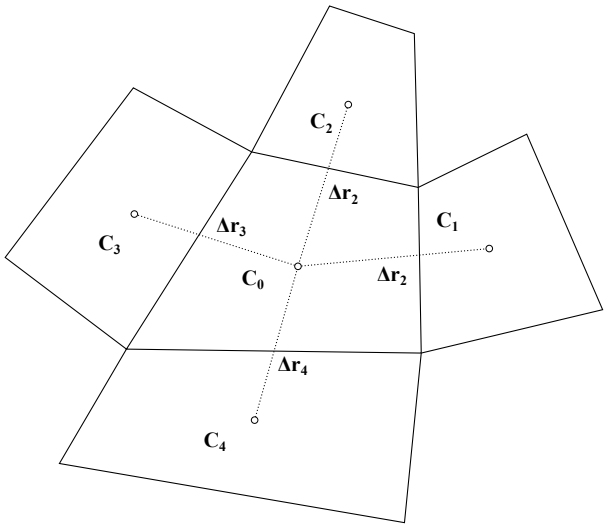

Figure 3.2: Gradient calculation at the centroid of cell C_0.

should be minimized in terms of RMS

$$R = \sum_j R_j. \tag{3.21}$$

This minimized value is achieved when differentiate of R with respect of components of gradient vector is 0:

$$\begin{array}{l} \dfrac{\partial R}{\partial a} = 0 \\ \dfrac{\partial R}{\partial b} = 0 \end{array}, \tag{3.22}$$

where $a = \frac{\partial \phi}{\partial x}|_0$, $b = \frac{\partial \phi}{\partial y}|_0$. Substitute equation 3.22 in equation 3.16, we have

$$\mathbf{M^T M d} = \mathbf{M^T \Delta} \phi, \tag{3.23}$$

which represents 2 equations with 2 unknowns. From this equation, we can solve for the gradient of ϕ located at the cell centroid.

In VISVE, the vorticity gradient is solved using least squares method. This gradient is then used in the correction of the diffusive term in non-orthogonal mesh as discussed in the previous section.

3.5 Vorticity-Velocity Solver

The velocity decomposition can be written as

$$\mathbf{q} = \mathbf{U}_\infty + \mathbf{u_p} + \mathbf{u}_\omega, \tag{3.24}$$

where total velocity field $\mathbf{q}$ is decomposed in to three components, incoming flow velocity $\mathbf{U}_\infty$, perturbation flow velocity $\mathbf{u_p}$ of the irrotational flow and the induce velocity $\mathbf{u}_\omega$ due to the vorticity field. The perturbation velocity $\mathbf{u_p} = \nabla\phi$ according to the velocity potential's definition.

When both the non-slip boundary and non-penetrate boundary are satisfied, the perturbation potential ϕ vanishes. Therefore we have

$$\mathbf{q} = \mathbf{U}_\infty + \mathbf{u}_\omega. \tag{3.25}$$

According to the definition of vector stream function $\boldsymbol{\psi}$:

$$\nabla \times \boldsymbol{\psi} = \mathbf{q}. \tag{3.26}$$

Write equation 3.26 using vorticity definition:

$$\nabla \times (\nabla \times \boldsymbol{\psi}) = \boldsymbol{\omega}, \tag{3.27}$$

which leads to

$$\nabla^2 \boldsymbol{\psi} = -\boldsymbol{\omega}. \tag{3.28}$$

In 2D we have a scalar equation

$$\nabla^2 \psi = -\omega. \tag{3.29}$$

The Poisson equation 3.29 can be solve using Green's function for Laplacian infree space:

$$\psi\left(\mathbf{x}_f\right) = -\int_{\Omega_C} \omega\left(\mathbf{x}\right) G\left(\mathbf{x}, \mathbf{x}_f\right)\, d\Omega + \psi_b, \tag{3.30}$$

where Ω_C is the computational domain; $\mathbf{x}_f$ is the field point and $\mathbf{x}$ is the dummy variable running over Ω_C; $G\left(\mathbf{x}, \mathbf{x}_f\right) = \left(\ln \mid \mathbf{x} - \mathbf{x}_f \mid\right)/2\pi$ is the Green's function for Laplacian in 2D. $\psi_b = yU_{\infty,x} - xU_{\infty,y}$ is the stream function corresponding to the background flow.

A standard Finite Volume Method (FVM) can also be adopted to solve equation 3.29. Applying the Stokes theorem over a cell leads to

$$A\omega = -\sum \frac{\partial \psi}{\partial n_j} \Delta l_j, \tag{3.31}$$

where A is the area of the cell and δl_j's are the enclosing edges of the cell. More details can be found in Tian (2014) [26].

3.6 Boundary Conditions

3.6.1 Solid Boundary Condition

The non-slip boundary condition is enforced by a Boundary Element Method (BEM) solver [26]. The numerical treatment at the boundary in shown in Figure 3.6.1.

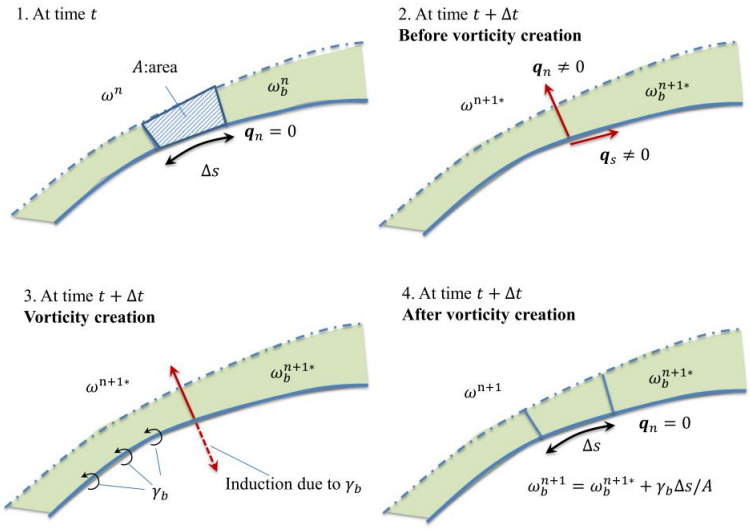

Figure 3.3: Schematic figure of the vorticity creation algorithm, from Tian (2014) [26].

1. Assume at the start of a time iteration at t, the velocity $\mathbf{q}$ and vorticity ω_b^n fields are calculated in the last iteration.

2. When we move on to next time step $t + \Delta t$, the VISVE solver solve the vorticity throughout the flow field using the velocity flow field calculated from the previous time step. Near the boundary, a vorticity ω_b^{n+1*} is assigned to the cell originally from VISVE. Since the vorticity field is known, the velocity could be evaluated using Biot-Savart law[14][26]. However, the non-slip and non-penetrate condition is not enforced on the boundary. Both the tangential velocity q_s and the normal velocity q_n are not diminished at this point.

3. A BEM solver is therefore called to enforce the solid boundary condition, by applying a sheet of concentrated vorticity γ_b on the boundary cells. γ_b induces another normal velocity which cancels out q_n so that the normal velocity diminishes at the boundary.

4. The vorticity sheet is then assign to the boundary cells, averaged by the panel area A, from which we get the new vorticity as

$$\omega_b^{n+1} = \omega_b^{n+1*} + \frac{\gamma_b}{A}. \tag{3.32}$$

The BEM solver locally corrects the non-slip boundary condition.

3.6.2 Outflow Condition

At the far field, the flow should be irrotational with zero vorticity, consistent with external free stream. Ideally the concentrated vorticity never reaches the far field boundary so that there's no induced velocity on the boundary.

However, small vorticity may still penetrate the boundary, especially in the wake due to diffusion. We use the Neumann condition at the boundary, which enforces the normal derivative at the boundary to be 0. Still, even if the Neumann condition is applied, boundary of the computational domain needs to be far enough in order to obtain a converged solution that is independent of the size of the domain.

A flow chart is helpful to understand the general procedure of VISVE. As shown in Figure 3.4, from the vorticity field of previous time step, we

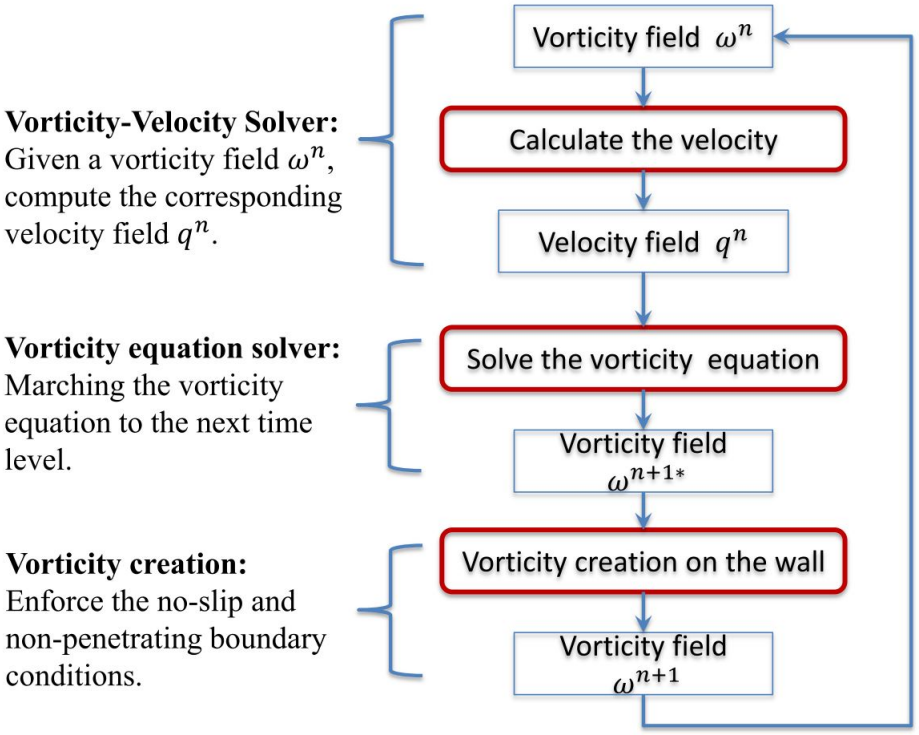

Figure 3.4: Flow chart of general procedure of VISVE, taken from Tian (2014) [26].

calculate velocity by solving Poisson equation 3.29. Then, using the velocity we calculated, we solve the vorticity transport equation 3.3 in order to obtain ω_b^{n+1*}. Applying BEM and assigning the vortex sheet γ_b to the boundary vorticity, we obtain the vorticity solution ω_b^{n+1}.

3.7 Calculation of Surface Pressure and Body Forces

The pressure term does not appear explicitly in vorticity transport equation 3.3. Therefore, pressure calculation is a post-processing of the worticity solver of VISVE.

An integral method was mentioned by Tian [26]. He define the total head H as:

$$H = \frac{q_r^2}{2} + p - \frac{\Omega^2 r^2}{2}, \tag{3.33}$$

where Ω is the rotational speed. q_r is the velocity in the rotational frame of reference of the propeller. Using momentum equation in the rotational frame of reference, the terms in 3.33 can be written in terms of q_r and ω:

$$\nabla H = \frac{\partial \mathbf{q}_r}{\partial t} + \mathbf{q}_r \times \boldsymbol{\omega} - \nu \nabla \times (\nabla \times \omega)\,. \tag{3.34}$$

Integrating the RHS of 3.34, gives H, and consequently, the pressure p. Also there are certain relation between velocity potential ϕ and total head H. More details are discussed in Tian [26].

Another integration model for pressure was developed in 2D by Wu [31]. The total head H is defined as:

$$H = \frac{q^2}{2} + \frac{p}{\rho}. \tag{3.35}$$

Using vorticity transport equation, the gradient of total head H can be written as:

$$\nabla H = -\frac{\partial \mathbf{q}}{\partial t} + \mathbf{q} \times \boldsymbol{\omega} - \nu \nabla \times \boldsymbol{\omega}. \tag{3.36}$$

Using the relationship between total head H and pressure p, pressure throughout the fluid domain can be solved.

In this work, the pressure model developed by Qian and Vezza (2001) [22] is used.

In viscous flow, non-slip boundary condition is valid on the cylinder surface. Therefore, in equation 3.1, the time derivative term $\frac{\partial \mathbf{q}}{\partial t}$ and the convection term $(\mathbf{q} \cdot \nabla)\,\mathbf{q}$ vanish at the surface. The diffusion term $\nu \nabla^2 \mathbf{q}$ can be written as $\nu \nabla \times \boldsymbol{\omega}$ according to the definition of vorticity. Equation 3.1 can be written as

$$\frac{\nabla p}{\rho} = \nu \nabla \times \boldsymbol{\omega}. \tag{3.37}$$

In 2D polar coordinate system, equation 3.37 can be written as

$$\frac{1}{r}\frac{\partial p}{\partial \theta} = -\mu \frac{\partial \omega}{\partial r}. \tag{3.38}$$

Assuming a local coordinate on the cylinder surface, s as the tangential direction and n as the normal direction, we have

$$\frac{\partial p}{\partial s} = -\mu \frac{\partial \omega}{\partial n}. \tag{3.39}$$

For each panel on the cylinder's surface, we can write equation 3.39 as

$$\frac{p_j - p_{j-1}}{\Delta s} = -\mu \left(\nabla \omega\right) \cdot \boldsymbol{e}_n, \tag{3.40}$$

where vorticity derivative in the n direction $\frac{\partial \omega}{\partial n}$ is written in a gradient form. After the non-slip boundary condition is implemented, the vorticity gradient at the boundary, i.e. the rate of vorticity generation, can be calculated. Therefore the surface pressure changes across each panel can be evaluated.

Pressure at the stagnation point at the leading edge of the cylinder can be easily determined using Bernoulli Equation. The stagnation gauge pressure, according to Bernoulli Equation, is $\frac{1}{2}\rho U_\infty^2$. After determine the stagnation pressure, surface pressure along the boundary can be determined using equation 3.40.

The viscous sheer stress τ on the surface is usually written as

$$\tau = \mu \frac{\partial u}{\partial n}, \tag{3.41}$$

where u is the tangential velocity parallel to the surface, and n is the unit normal vector. Although it is a 1D equation, it can also apply to the cells near the boundary, when the distance to the surface is much smaller than the radius of curvature of the surface. Using the definition of vorticity ω, equation 3.41 can leads to

$$\tau = \mu\omega. \tag{3.42}$$

Note that the velocity normal to the boundary of the body is zero.

The drag and lift force can be therefore determined using the surface pressure and shear stress [22]:

$$D = R \oint_{bs} \left(\mu R \frac{\partial \omega}{\partial n} - \mu\omega \right) \sin\theta \mathrm{d}\theta \tag{3.43}$$

$$L = R \oint_{bs} \left(\mu R \frac{\partial \omega}{\partial n} - \mu \omega \right) \cos\theta \mathrm{d}\theta \tag{3.44}$$

where bs denotes the body surface. Non-dimensional drag and lift coefficients can be obtained by

$$C_d = \frac{D}{\rho U_\infty^2 R} \tag{3.45}$$

and

$$C_l = \frac{L}{\rho U_\infty^2 R} \tag{3.46}$$

where R is the radius of the cylinder and ρ is the density of the fluid.

Chapter 4

Application on Flow around Cylinder

4.1 Impulsively started cylinder flow

The impulsively started cylinder flow is an ideal start condition flow that can't be created in experiment. A rapid start of flow in experimental works could be considered as a sufficient simulation.

However, in numerical study, ideally impulsive start is possible. At $t = 0^+$, the sudden start of the flow is simulated by the potential flow, with slip condition on the solid surface of the cylinder. The velocity on the boundary brings a strong shear stress, generating a thin layer of high vorticity in the next time step. At $t = \Delta t$ the first time step, non-slip boundary is enforced by the vorticity on the surface. Then this vortex sheet becomes vorticity flux and comes into the fluid field by convection and diffusive process.

The challenges in this separated flow are usually:

1. The time evolution of the flow field. At different Reynolds numbers, the process of vortex generation and its convection in the wake region are particularly sensitive to the grid and the numerical scheme.

2. The application of the boundary condition at the start of the flow. The physics of a sudden start indicates that the solid boundary transforms

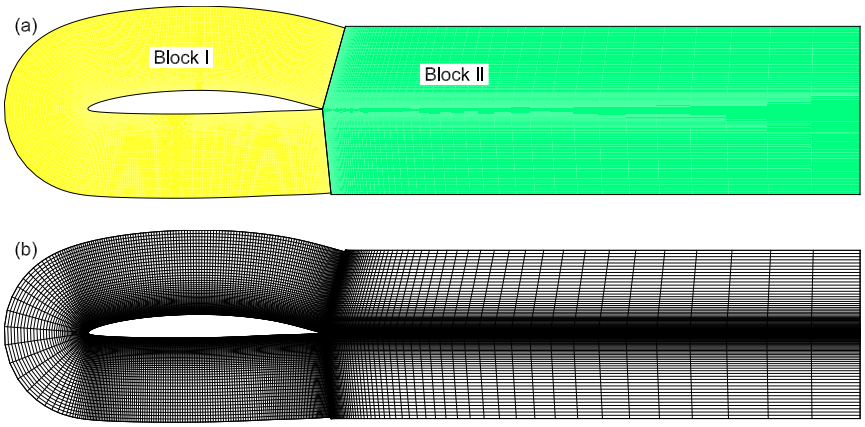

Figure 4.1: Two block griding for flow around a hydrofoil [26]. (a) Block I and Block II cover the front area and wake area, respectively. (b) Expanding meshes around the foil.

from slip condition into non-slip condition rapidly. Resolving this transformation of boundary condition is especially crucial to our simulation.

4.2 Griding scheme

4.2.1 Body-fitting griding over hydrofoil with small trailing edge angle

Original VISVE creates a body-fitting mesh around the hydrofoil, which consists of two parts of mesh blocks as shown Figure 4.1.

The first mesh block covers the region around the surface of the hydrofoil. It develops according to size of the panels on the foil and expands with an expansion ratio in the radial direction perpendicular to the panels. At the trailing edge, since the trailing edge angle τ is small, the angle between the grid on the upper surface and lower surface $\pi - \tau$ is close to π, leaving a blank

region in the wake.

The second mesh block covers the region in the wake, connecting continuously with the first block. Its first layer keeps the size of the mesh at tailing edge and then expands with an expansion ratio to cover the wake region.

This mesh gives a good resolution closed to the surface of the foil and in the wake region, which ensures the resolution of the domain where the vorticity generates and develops. Since the vorticity is zero away from the foil, Block I provides a good coverage of the thin region around the surface, saving the computation cost so that finer mesh can be used close to the foil and in the wake.

The interface of Block I and Block II is not absolutely smooth in the term of the density of the cells. However this discontinuity is negligible due to the fact that the trailing edge angle τ is small and the angle between the Block I's upper surface and lower surface is close to π. Thus, although the mesh is unstructured, it can still be treated as structured mesh within some accuracy requirements.

4.2.2 Griding over cylinder

The griding scheme needs to be modified when applying to a cylinder.

If the same scheme that generates Block I is used, at the trailing edge of the cylinder, the mesh is perpendicular to the surface panel, leaving no blank in the wake region. This will result in a polar grid around the cylinder, as shown in Figure 4.2, covering the region both around the cylinder and in the

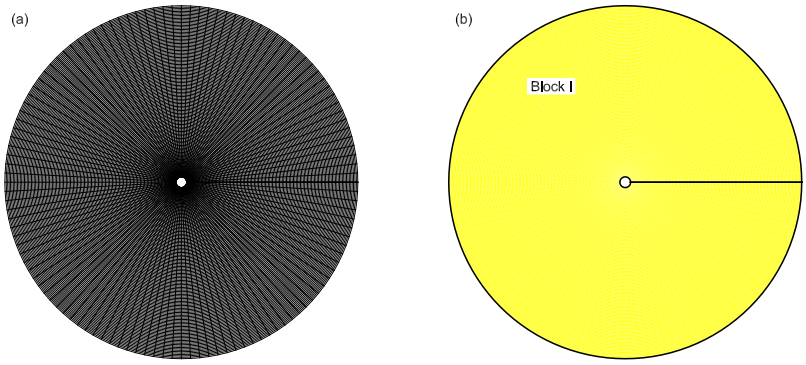

Figure 4.2: One block griding for cylinder flow. (a) Mesh with expansion in radial direction. (b) Only one block overs the whole domain.

wake. In this case, since the wake region has already been covered, Block II is not needed anymore.

This griding scheme is usable: it covers the computational region that we are interested in. However, in order to resolve the wake region, this polar grid needs to have a large radius, which means that it should also cover the same span around the cylinder as the span in the wake. This leads to a consequence of wasting cell in the region that we are not interested in, where away from the cylinder in front of the wake, the vorticity is zero everywhere.

Thus, a new griding scheme needs to be created. It should cover a thin region around the cylinder, providing a good resolution closed to the surface where the vorticity is generated; At the same time, it should also provide a extendable grid in the wake, so that we could resolve the vortex shedding patterns in the downstream.

Therefore, another two-block griding is created, shown in Figure 4.3.

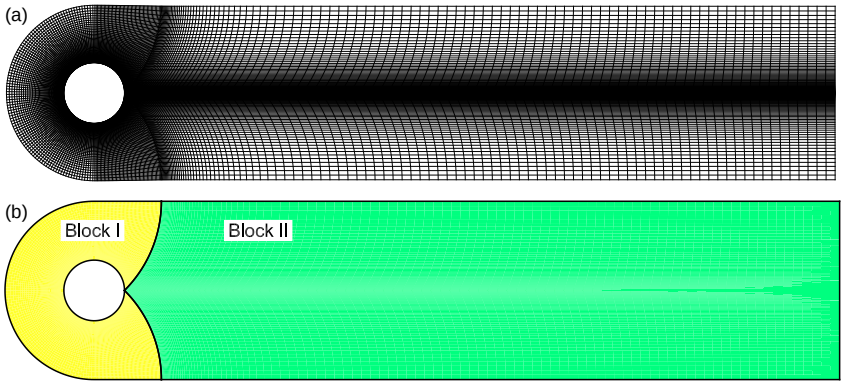

Figure 4.3: Two block griding for cylinder flow. (a) Expanding meshes around the cylinder. (b) Block I and Block II cover the front area and wake area, respectively.

The first block still covers a region close to the surface of the cylinder, while an angle between the mesh on the upper and lower is created, leaving the space for second block to cover the wake region. The first layer of cells of Block II keeps the size at the interface with Block I, and expand into the wake with an expansion region.

Block I consists of two parts: a polar region in front half and a twisted region in the rear part. In the polar grid, the meshes expand in the radical direction perpendicular to the panels. In the twisted region, at the top and the bottom of the cylinder, the mesh expands in the radical direction, but at the trialing edge, the meshes first developed in 45 degree to the trailing edge panel, then though an arc line, gradually turn to parallel to the panel, perpendicular to the horizontal mesh boundary. The inner meshes are generated using coons

patch scheme, providing a smooth bi-linear blending griding in between.

The new two-blocks griding scheme provides a good coverage both around the cylinder and in the wake, as well as the flexibility in refining the grids close to the surface and in the wake area, while not wasting any unnecessary meshes in the region where the vorticity is zero.

The griding scheme leads to a problem at the interface between Block I and II, with twisted grids in both blocks. The mesh can no longer be considered as orthogonal mesh, as the skewness is significant in this body-fitting griding. Thus the solver needs to be modified in order to include the effect of the skewness in this griding.

4.3 Parallel computing

The VISVE method can be fully parallelized. Parallelization of the code can significantly shorten the computational time experienced by end-users.

OpenMP was implemented in the code. The most time consuming step is the vorticity-velocity solver where the volume integral with the point source kernel is performed [26], which is parallelized by OpemMP. An efficiency test has been done, and the results are included in the next chapter.

Chapter 5

Results and Discussion

In this chapter, the results of impulsively started flow are presented at different Reynolds number($Re = \frac{\rho VD}{\nu}$). The time evolution of the flow features were also analyzed with respect to characteristic time $T = Ut/R$.

5.1 Grid and Domain Independence

In order to evaluate the influence of the grid domain and the grid density on the solution, three sets of tests have been calculated for cylinder flow at $Re = 1000$.

5.1.1 Sufficiency of Computational Domain

One of the most important advantage of VISVE compared with other Navier-Stokes (N-S) equations solver is that it uses smaller computational domain due to the concentration of the vorticity. The computational domain boundary of a N-S solver needs to be far away from the object, in some cases several cylinder diameters away, so that the velocity reaches the far field condition. Solid boundary or far field boundary could be applied in a N-S solver since the effect of the boundary is small once the domain is sufficiently large.

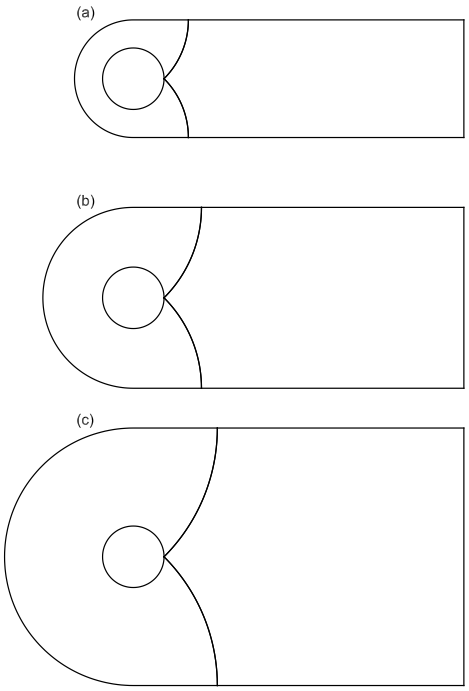

Figure 5.1: Computational domain used in domain sufficiency test: (a) Domain height = $2D$, radial cells num = 65.(b) Domain height = $3D$, radial cells num = 80. (c) Domain height = $4D$, radial cells num = 90.

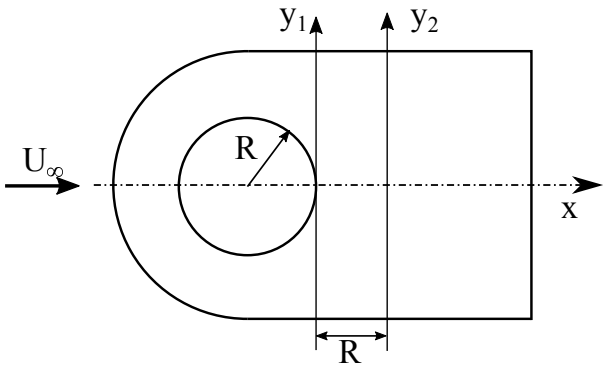

Figure 5.2: The velocity profile location used in the domain and gird independence tests. Vertical line y_1 lies right behind the cylinder and vertical line y_2 lies one radius behind the cylinder.

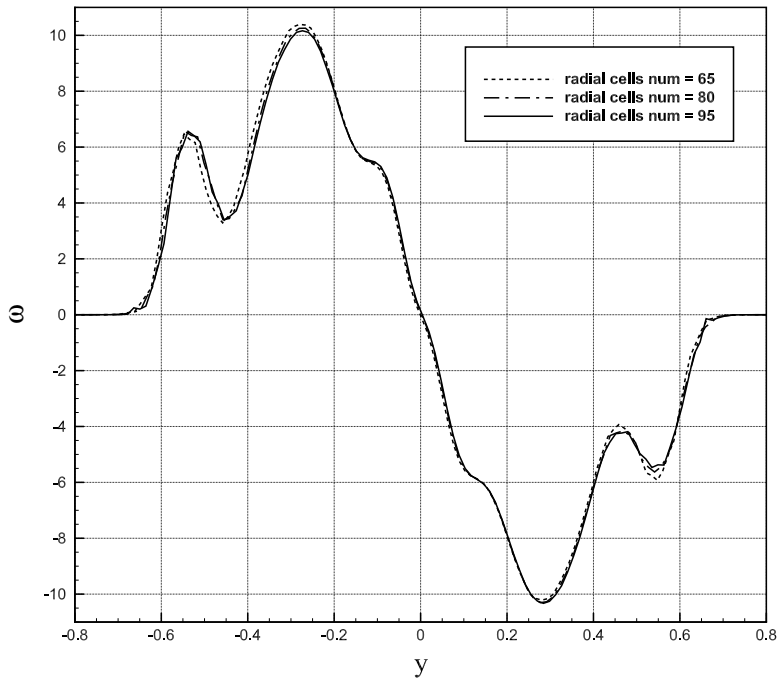

Figure 5.3: Domain effect on the vorticity y_2 on vertical line one radius behind the cylinder at $T = 5.0$.

However, a vortex method solver only needs the domain to cover the rotational flow. In the cylinder flow, the domain of the rotational flow in VISVE is significantly smaller than the domain for a N-S solver. Therefore, in order to know whether the domain is large enough for converged solution, a test on the sufficiency of the computational domain is necessary for this method.

In order to find a suitable size of the domain, the grid sizes of the first layer and the expansion ratio are the same for all the cases, while the number of grids are different. In the first test, 65 cells are used in the radial direction so we have a domain with a height of $2D$. Instead of changing the size of the cells, more cells are added in the radial direction in the other two tests, so that we have a domain with a height of $3D$ and $4D$, with 80 and 90 cells in the radial direction, respectively. Figure 5.3 shows the vorticity on the vertical line y_2 in the wake one radius behind the cylinder with different computational domain at $T = 5.0$. The small discrepancy indicates the domain is large enough to capture all the flow structures for the Reynolds number considered.

5.1.2 Grid Independence

Another set of tests were focus on the effects of density of the panels on the surface of the cylinder. The number of the cells on the radial direction is kept as 80 and the number of panels on the surface is 100, 200 and 300, respectively. In Figure 5.4, the vorticity on the vertical line y_1 right behind the cylinder were ploted at $T = 2.5$. The small differences between the profiles indicate that the density of the surface panel is fine enough to resolve the flow

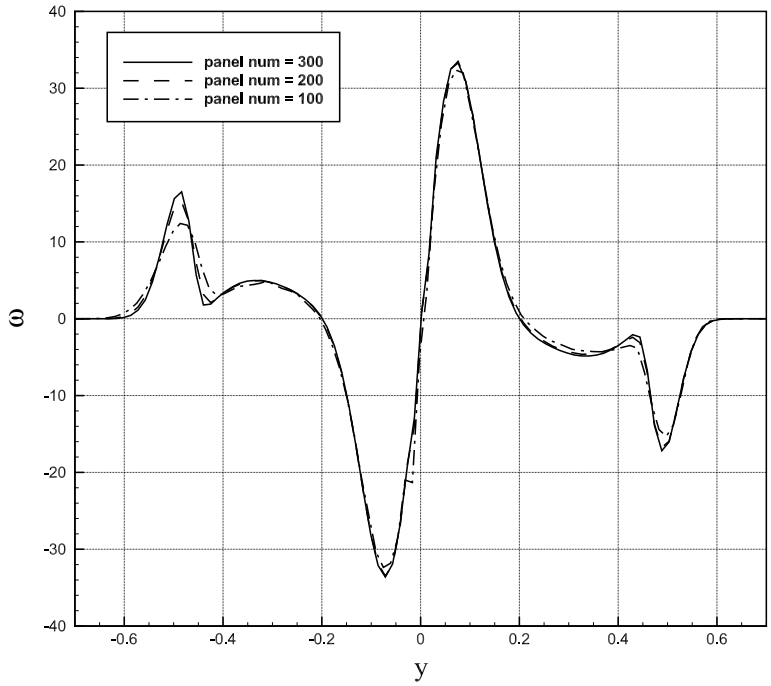

Figure 5.4: Effects of density of the surface panel to the vorticity on the vertical line y_1 right behind the cylinder at $T = 2.5$.

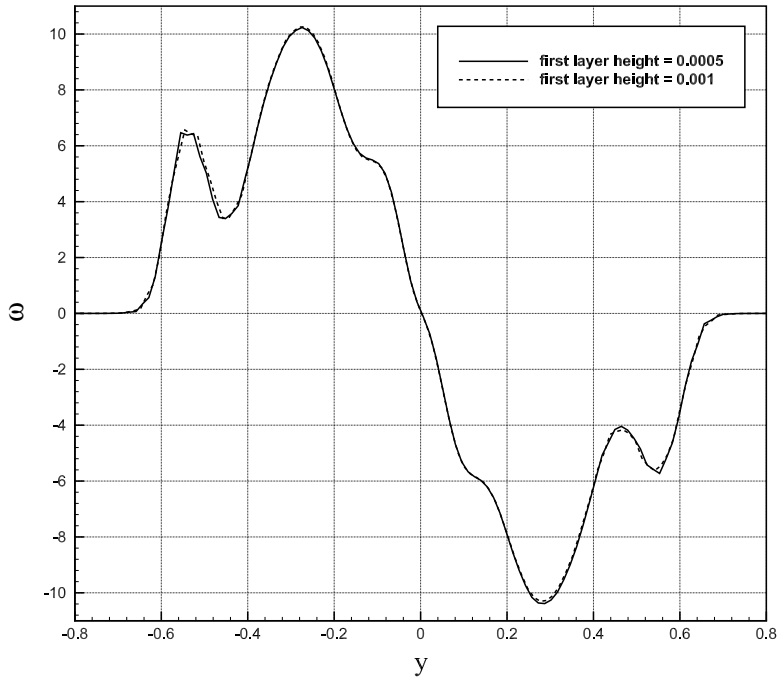

Figure 5.5: Effects of density of the radial cells to the vorticity on the vertical line y_2 right behind the cylinder at $T = 5.0$, with different height of the first layer of the mesh near the surface.

structures for the $Re = 1000$.

Similarly, a set of tests were conducted to evaluate the effects of density of the cells in the radial direction. The number of the panels on the cylinder surface is kept as 200 and the ratio of height of the first layer of cells to the diameter of the cylinder is 0.001 and 0.0005 respectively. The expansion ratio on the radial direction is kept as 1.05 in both cases and the total height of the domain is fixed. In Figure 5.5, the vorticity on the vertical line y_2 one radius behind the cylinder were ploted at $T = 5.0$. The small differences between the profiles indicate that the density of the cells in radial direction is fine enough

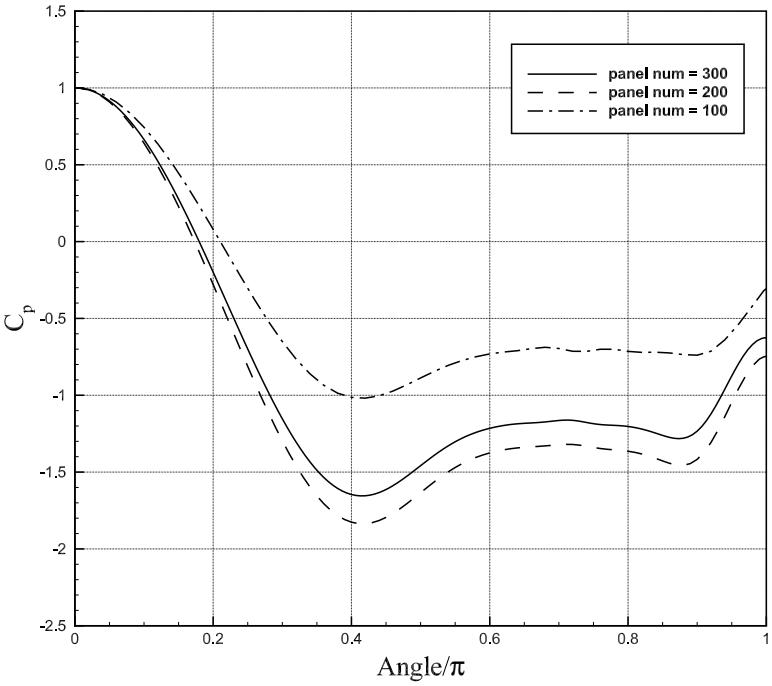

Figure 5.6: Effects of density of the surface panel on the pressure on the solid surface at $T = 5$.

to resolve the flow structures for the $Re = 1000$.

The new surface pressure model is especially sensitive to the number of panels on the solid boundary, since it is a post process of the VISVE solver, and the error accumulates through the integration path. Figure 5.6 presents the pressure sensitivity to the panel number, as the profile changes while the density changes. At panel number = 300, the pressure is close to convergence compared with the other two profiles. More tests need to be done in future works.

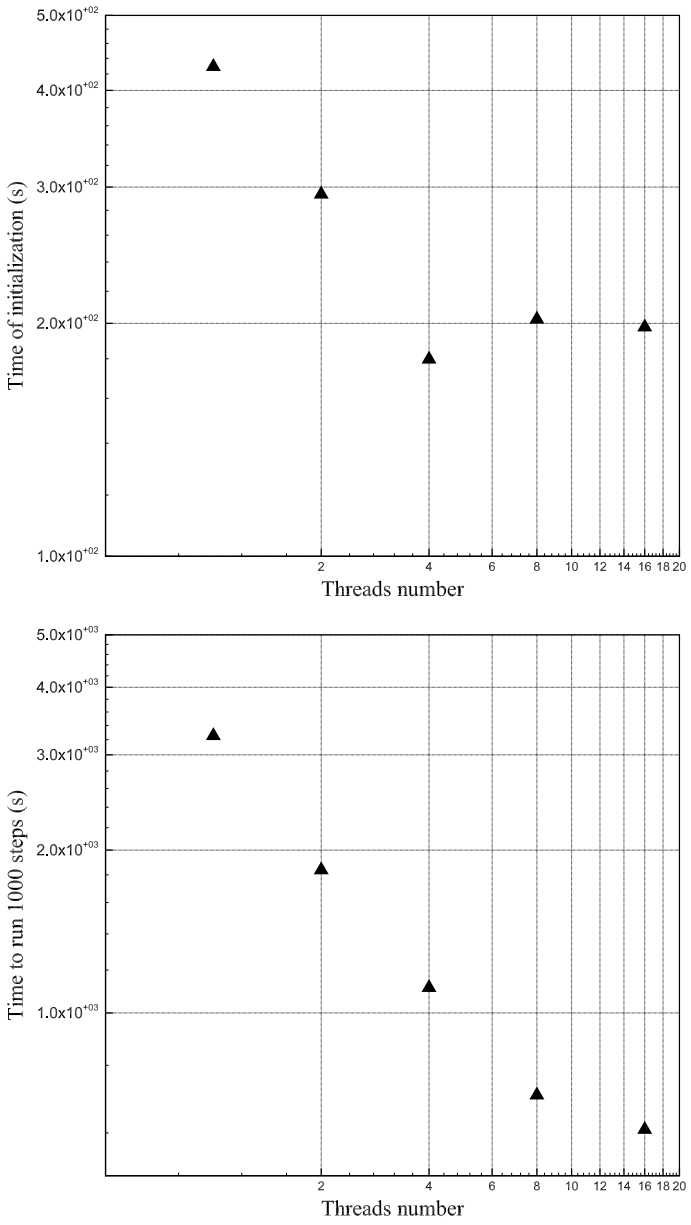

Figure 5.7: Benchmarking of case of 24,000 mesh with different number of threads.

5.2 Computational Efficiency

The computational efficiency are improved by the parallelism of the code. OpenMP is implemented in the current software so that multiple threads can be used to calculation. Figure 5.7 presents the bench-marking of parallel code, in which the time of initialization of the code before the time step iterations, and the time it takes to do 1,000 time steps iterations are both tested.

The bench-marking were conducted with a 24,000 mesh using 1, 2, 4, 8, 16 threads on one node. It can be observed from the plots that, as the threads number increases, the time of iteration over time steps reduced exponentially, while the initialization time doesn't change much when the number of threads exceeds 4. This was because of that the memory allocation takes up most of the initialization process.

The bench-marking was conducted on the server of Texas Advanced Computing Center (TACC), at the University of Texas at Austin.

5.3 Impulsive Start Results

The impulsive start cylinder flow is simulated with different Reynolds number ($Re = U_\infty D/\nu$). In this thesis, Re is selected to be 1000, 3000, and 9500 respectively. In this section, we presents the flow properties of the flow before Vortex Induced Vibration (VIV). We used 200×80 in Block I (200 panels on the cylinder and 80 cells in the radial direction) and 160 in Block

II (extending 50 cells from the rear interface of Block I). The time step used this work is 0.0005.

5.3.1 Flow at Re=1000

Figure 5.8 shows the time evolution of the streamline and vorticity contours at $Re = 1000$. The α-phenomena can be observed in the simulation. A pair of primary vortices are formed at $T = 1.0$ and gradually increase its span as time increases, while a pair of secondary vortex appears as a thin layer at first and then grows stronger. However this pair of secondary vortices remain bounded by the primary vortices and stable beyond $T = 5.0$, never reaching the outside irrotational flow.

In figure 5.9, comparison of the vorticity on the cylinder surface is presented with the numerical data from Qian and Vezza [22]. The results are in good agreement. In Figure 5.10, vorticity on the surface is presented at different time steps. The evolution of the vorticity generation at the thin boundary layer at the surface can be observed. The vorticity at the front are gradually diffused and flushed downstream, as the secondary vortices generated from the inner layer and interact with the primary vortices. The separation point moves upstream due to the increasing intensity of the secondary vortex.

The radial velocity profiles along the rear centre line of the cylinder at different time steps are presented in Figure 5.11. The profiles show that the intensity of the primary vortex increases as time increases, and the stagnation point moves downstream as the vortex expands.

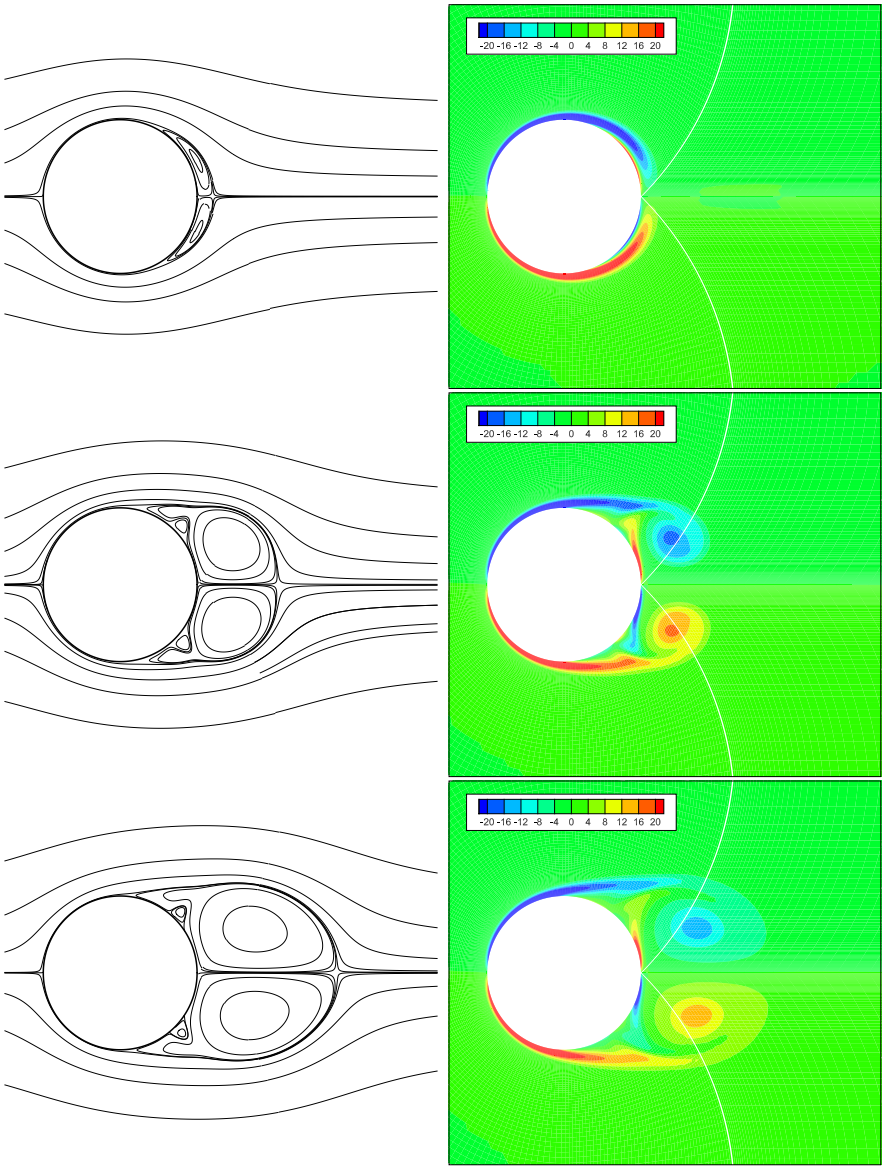

Figure 5.8: Instantaneous streamlines (left) and vorticity contours (right) for $Re = 1000$ at $T = 1.0, 3.0, 5.0$, predicted by current method. Notice that even though there is grid discontinuity at the block interface, the solution is smooth through the interface.

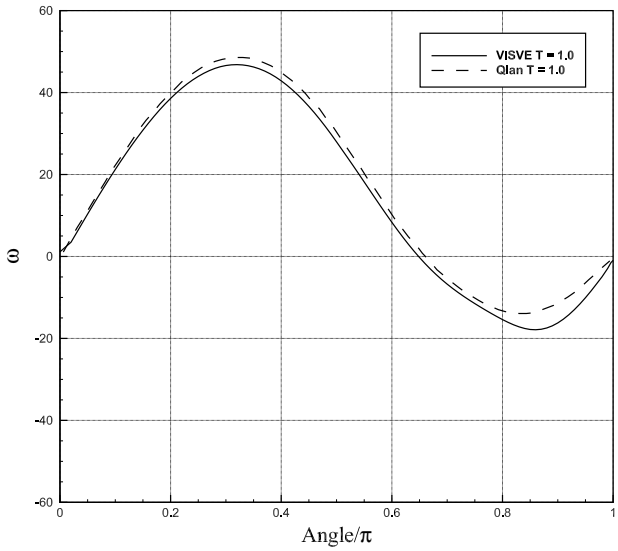

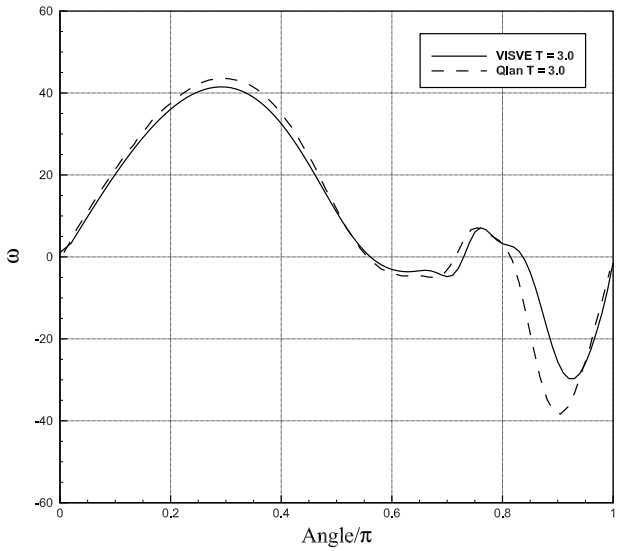

Figure 5.9: Surface vorticity distribution for $Re = 1000$ at $T = 1.0, 3.0$ (numerical data of Qian and Vezza (2001) [22]).

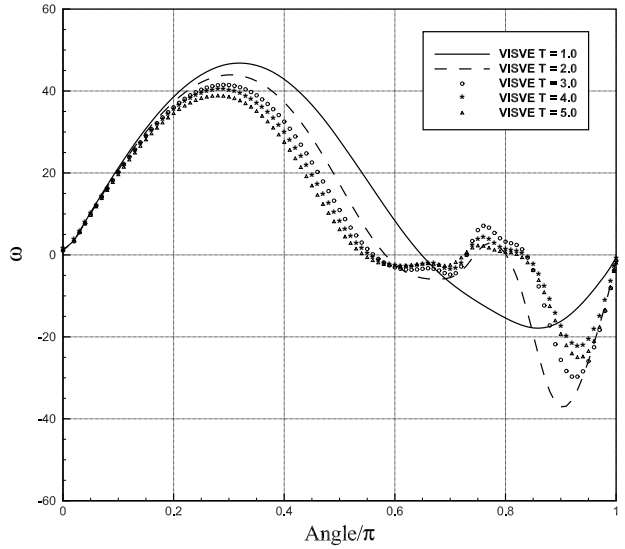

Figure 5.10: Time variation of the surface vorticity distribution: $Re = 1000$

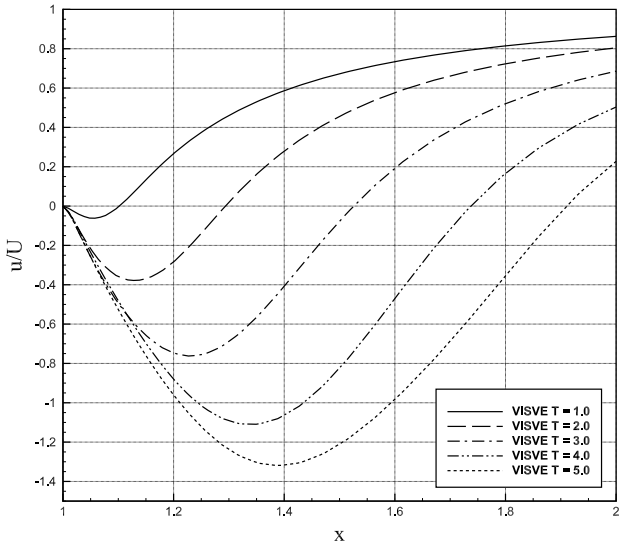

Figure 5.11: Radial velocity distribution along the rear centerline of the circular cylinder at $Re = 1000$.

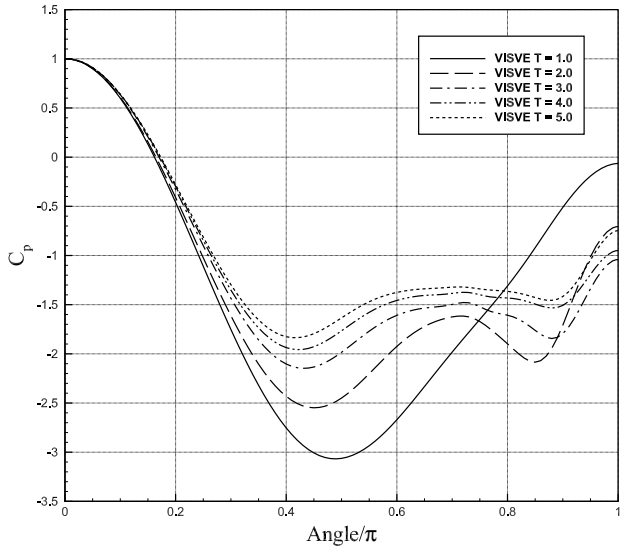

Figure 5.12: Time variation of the surface pressure coefficient for $Re = 1000$.

In Figure 5.12, we present the evolution of surface pressure coefficient at $Re = 1000$. At $T = 1.0$ the pressure coefficient has its minimum value around the midpoint where the maximum velocity appears. As the start-up primary vortex diffuses and moves to downstream, the pressure coefficient increases.

5.3.2 Flow at Re=3000

Figure 5.13 give the time evolution of the streamline and vorticity contours at $Re = 3000$. The α-phenomena can also be observed in the simulation. Noticing that there are only 2 pairs of vortices generated in the flow field and the secondary vortex never reaches the outflow. We will see a different phenomena at $Re = 9500$ in the next section.

In Figure 5.14, comparison of the vorticity on the cylinder surface is

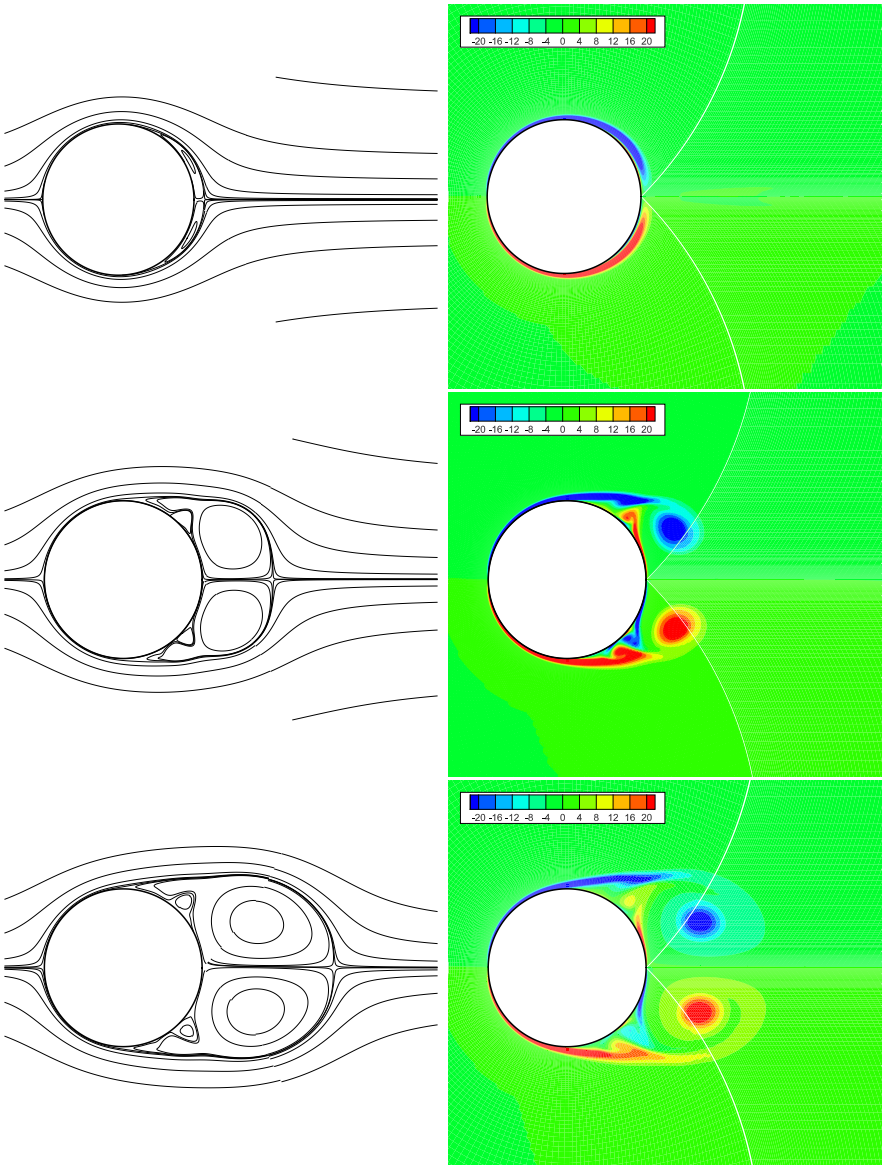

Figure 5.13: Instantaneous streamlines (left) and vorticity contours (right) for $Re = 3000$ at $T = 1.0, 3.0, 5.0$, predicted by the current methods. Notice that even though there is grid discontinuity at the block interface, the solution is smooth through the interface.

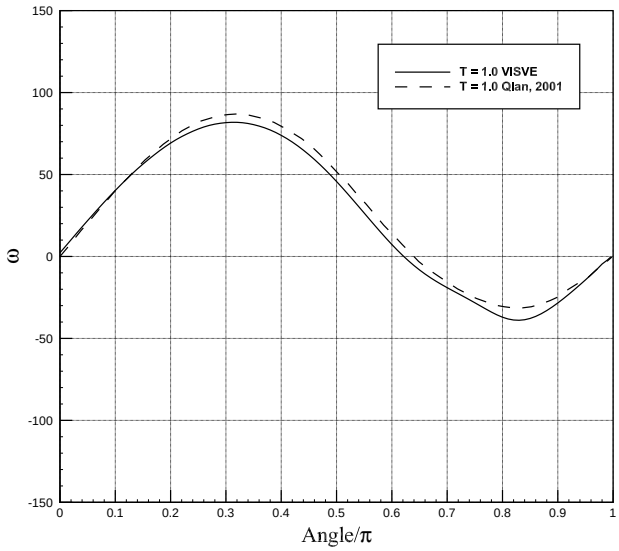

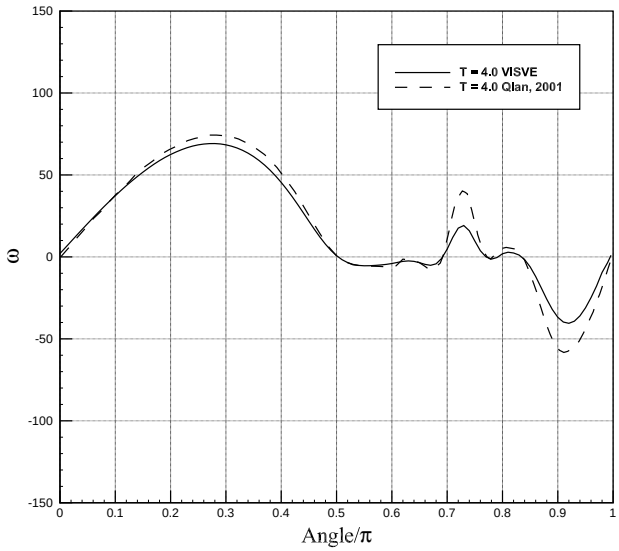

Figure 5.14: Surface vorticity distribution for $Re = 3000$ at $T = 1.0, 4.0$ (numerical data of Qian and Vezza (2001) [22]).

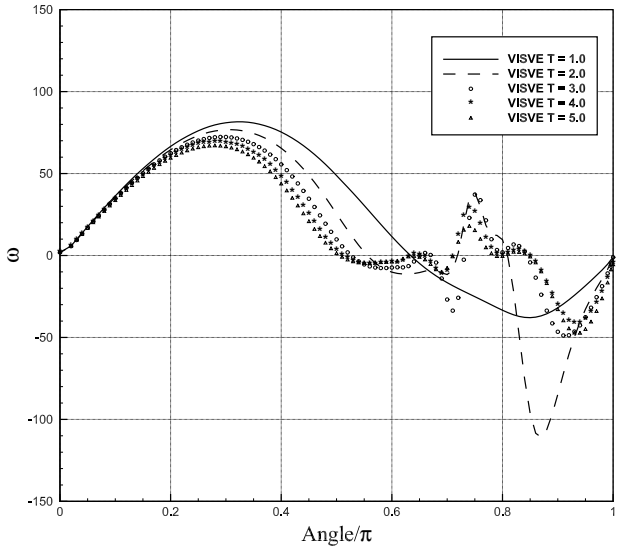

Figure 5.15: Time variation of the surface vorticity distribution: $Re = 3000$

presented with the numerical data from Qian and Vezza (2001) [22]. The results are in good agreement, except when angel is larger than 0.7π, the intensity of the surface vorticity is smaller than expected.

In Figure 5.15, vorticity on the surface are presented at different time steps. The evolution of the vorticity generation at the thin boundary layer at the surface can be observed. As shown in this figure, when angel is larger than 0.7π, the vorticity changes rapidly from $T = 1.0$ to $T = 2.0$. This rapid change might be sensitive to the size of the time step. More tests are recommended here.

The radial velocity profiles along the rear centre line of the cylinder at different time steps are presented in Figure 5.16, compared with experimental data by Bouard and Coutanceau (1908) [4]. The profiles show that the inten-

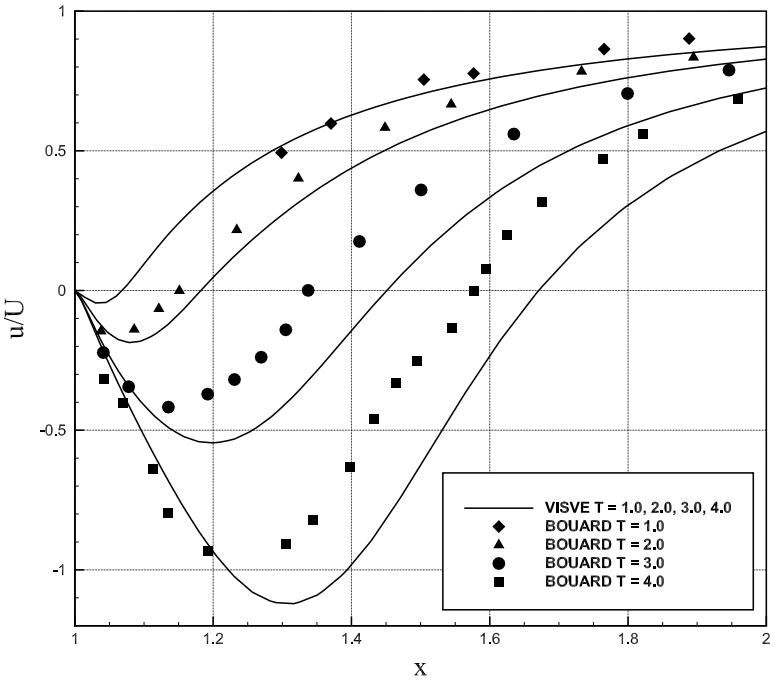

Figure 5.16: Radial velocity distribution along the rear centre line of the circular cylinder at $Re = 3000$ (experimental data of Bouard and Coutanceau (1980) [4]).

sity of the primary vortex increases as time increases, and the stagnation point moves downstream as the vortex expand. Discrepancy can be observed. The VISVE result seem to develop ahead of the time step in the flow visualization. Again, the vorticity field changes rapidly in the early stage. Secondary vortex is generated and becomes strong. Large time steps may leads into accumulating error as time increases.

Figure 5.17 compares the VISVE pressure distribution with results from Chang and Chern (1991)[5]. In the front part the pressure prediction is close to Chang and Chern's result, however when angel is larger than 0.6π, the intensity of pressure is higher than the published data. As we discussed in the previous section, the surface pressure model is slowly converging as the panel number increases, and using 200 panels, the pressure solution is not converged. This may be also caused by the discontinuity of the grid distribution at the interface of the two blocks.

In figure 5.18, we present the evolution of surface pressure coefficient at $Re = 3000$. At $T = 1.0$ the pressure coefficient has its minimum value at around the midpoint where the maximum velocity appears. As the start-up primary vortex diffuses and moves to downstream, the pressure coefficient increases and changes rapidly.

5.3.3 Flow at Re=9500

Figure 5.19 give the time evolution of the streamline and vorticity contours at $Re = 3000$. The β-phenomena can be observed in the simulation.

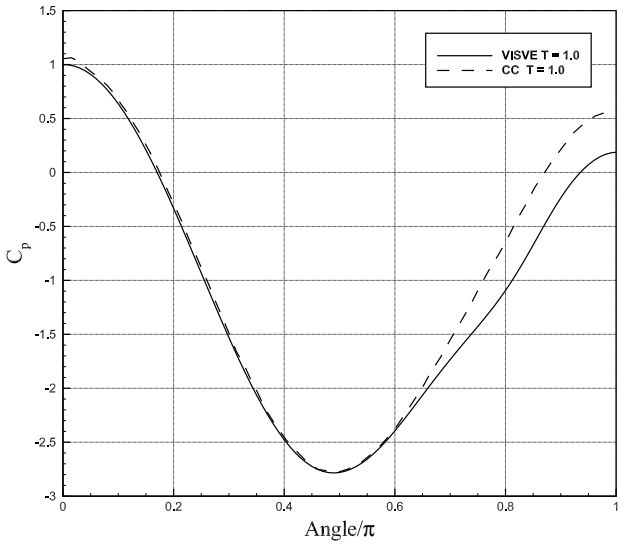

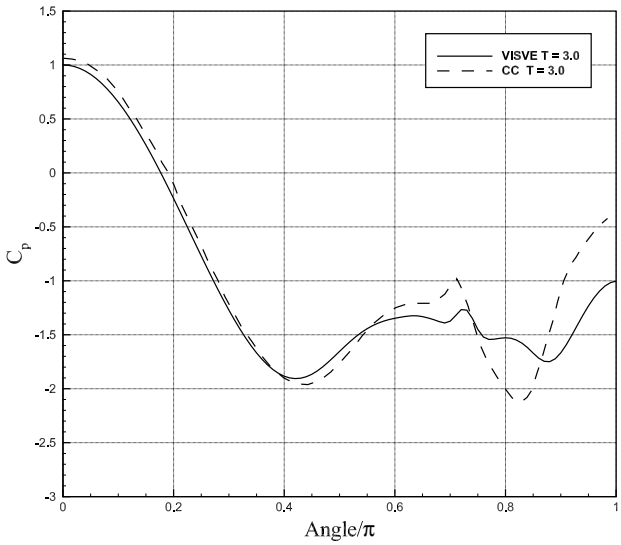

Figure 5.17: Time variation of the surface pressure coefficient for $Re = 3000$ at $T = 1.0, 3.0$ (numerical data of Chang and Chern (1991) [5]).

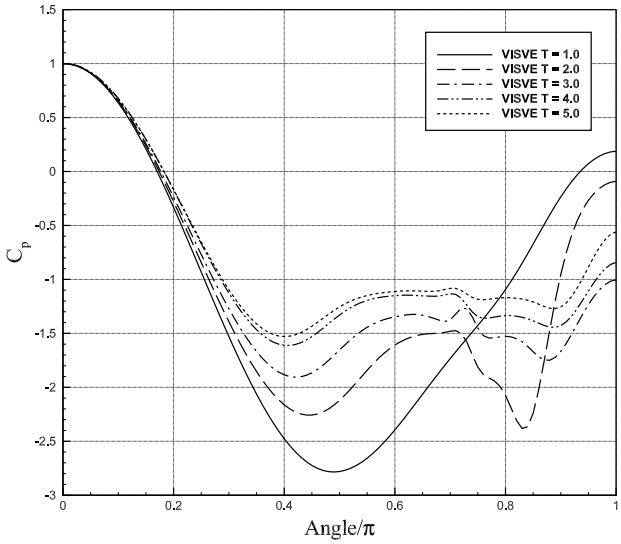

Figure 5.18: Time variation of the surface pressure coefficient for $Re = 3000$.

β-phenomena was first observed by Bouard and Coutanceau, using flow visualization, which is cited here in Figures 5.20-5.23. Initially a thin layer of vorticity ("forewake") is formed at the surface of cylinder. This forewake gradually forms the primary vortex and the core starts to separate into two vortices at $T = 1.5$ in Figure 5.20. At the same time, the secondary vortex is generated at the inner layer of the primary vortex.

The small vortex separated from the forewake becomes stronger and starts to detach from the primary vortex and the cylinder surface at $T = 2.0$. As shown in Figure 5.21, the detached vortex penetrates the bound of primary vortex and reaches the irrotational outer flow.

As the primary and secondary vortices becomes stronger, the angle between the detached vortices and the surface of the cylinder becomes larger

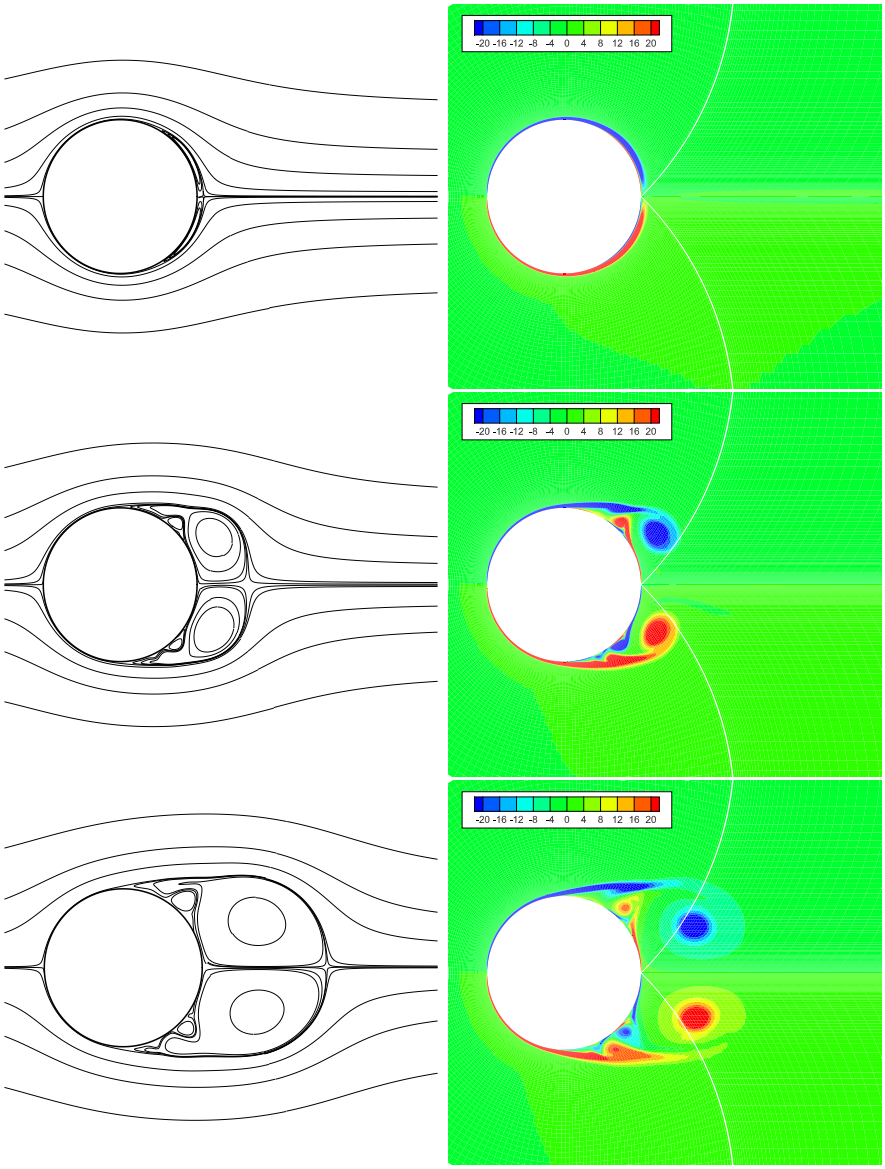

Figure 5.19: Instantaneous streamlines (left) and vorticity contours (right) for $Re = 9500$ at $T = 1.0, 3.0, 5.0$, predicted by current method. Notice that even though there is grid discontinuity at the block interface, the solution is smooth through the interface.

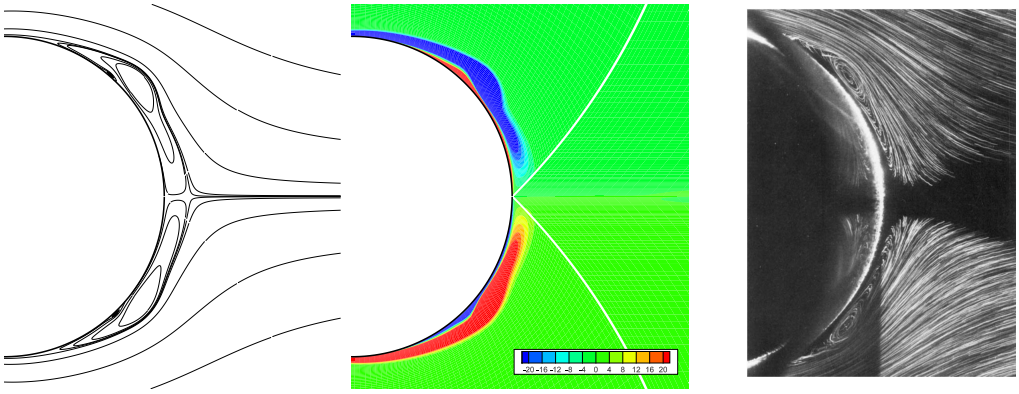

Figure 5.20: Comparison of the streamlines and vorticity patterns for $Re = 9500$ at $T = 1.5$ (flow visualization by Bouard and Coutanceau (1980) [4]). Before $T = 1.5$, the primary vortices are formed in a thin layer ("forewake"). At $T = 1.5$, the core of this primary vortex starts to separate.

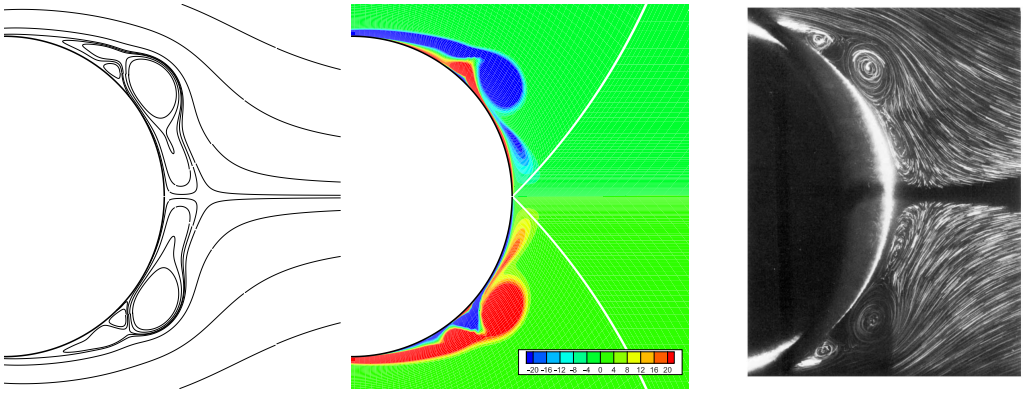

Figure 5.21: Comparison of the streamlines and vorticity patterns for $Re = 9500$ at $T = 2.0$ (flow visualization by Bouard, 1980[4]). At $T = 2.0$, a small vortex separated from the primary vortex.

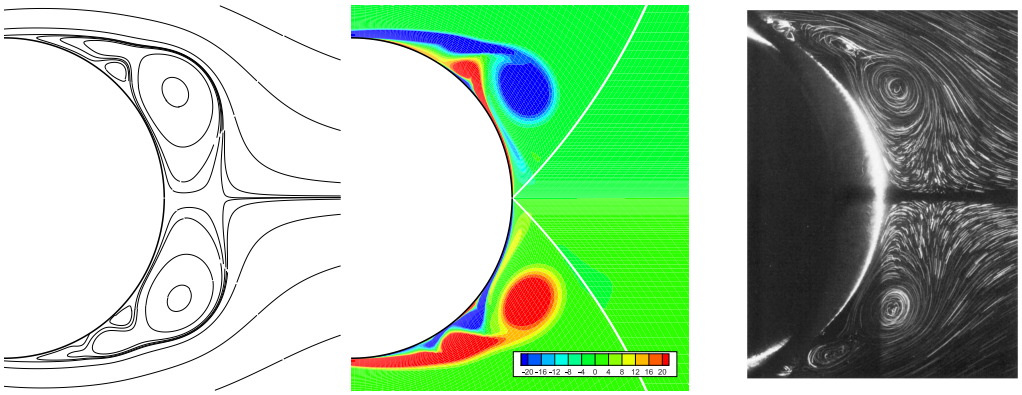

Figure 5.22: Comparison of the streamlines and vorticity patterns for $Re = 9500$ at $T = 2.5$ (flow visualization by Bouard, 1980[4]). At around $T = 2.5$, the small vortex separated from the forewake detaches from the surface of the cylinder and reaches the outflow.

as it flushes into the outer flow. In Figure 5.22, the intensity of the primary vortices are reduced and stretched by the detached vortices.

As the detached vortices are diffusing and detaching, they gradually merge into the primary vortices as they go downstream. At $T = 3.0$, in Figure 5.23, they diminish in the primary vortices, as the secondary vortices growing stronger but stabilizing at the inner layer of the flow, never reaching the outer flow.

From Figures 5.20-5.23, we could see the phenomena different from the α-phenomena in flow at $Re = 1000$ and $Re = 3000$, as they agree well with the experimental flow patterns.

In Figure 5.24, the surface vorticity at $T = 1.0, 3.0$ are presented. Notice that large discrepancy can be observed at $T = 3.0$, when angel is larger than 0.7π. Comparing with Figure 5.23, the secondary vortex was becoming

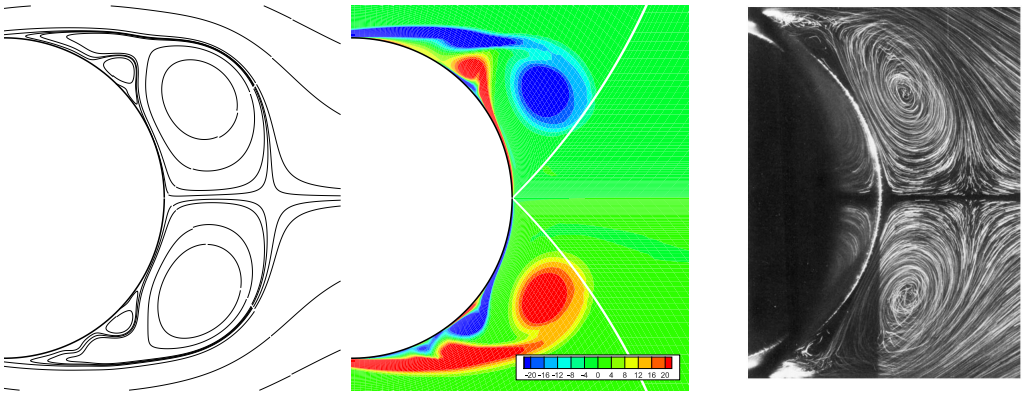

Figure 5.23: Comparison of the streamlines and vorticity patterns for $Re = 9500$ at $T = 3.0$ (flow visualization by Bouard, 1980[4]). At $T = 3.0$, the detached vortex merged into the primary vortex.

stronger at that time step and the vortex sheet is very strong and sensitive to the grid density.

Figure 5.26 presents the time evolution of the wake length, compared to experimental data. The result seem to be comparable to the experiment measurements, but somewhat larger than the data after $T = 2.5$. This might be caused by insufficiently small time step and the discontinuity in the grids.

In Figure 5.27, we present the evolution of the surface pressure coefficient at $Re = 9500$. As showed in Figures 5.20-5.23, there are very large changes of the pressure from time to time, and that indicates the strong interaction of the cylinder with the vortices in the wake region.

5.4 Long Time Solutions

In this section, long time solution are presented. We presents the flow properties of the flow after a stable Vortex Induced Vibration (VIV) estab-

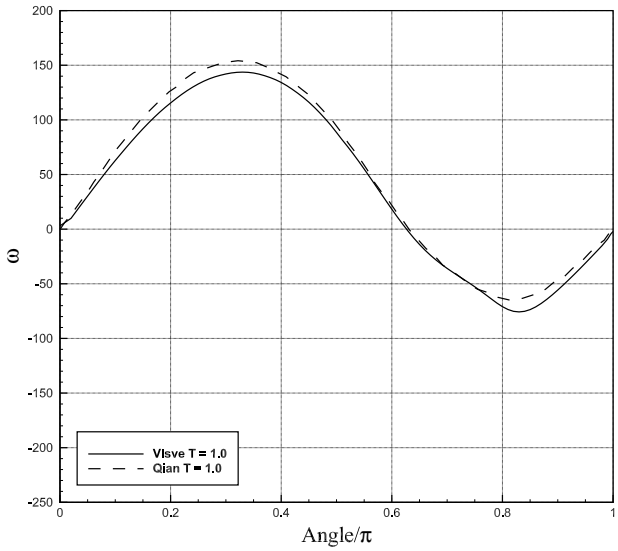

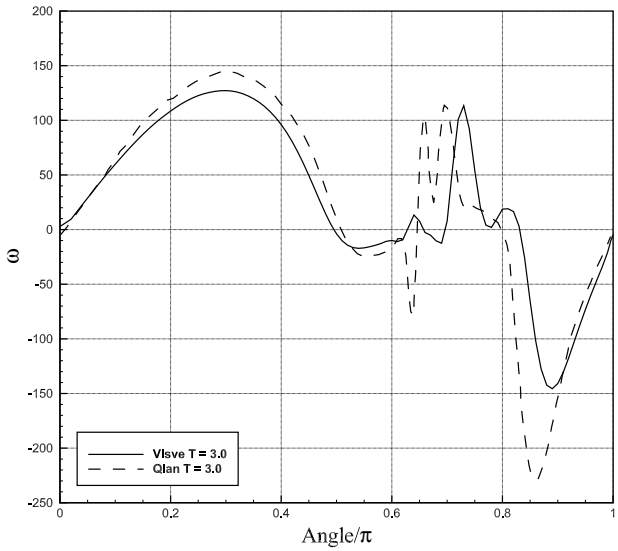

Figure 5.24: Surface vorticity distribution for $Re = 9500$ at $T = 3.0$ (numerical data of Qian, 2001[22]).

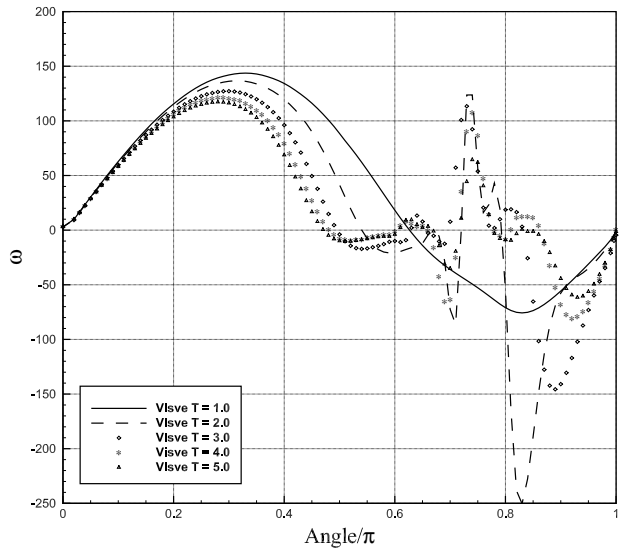

Figure 5.25: Time variation of the surface vorticity distribution: $Re = 9500$

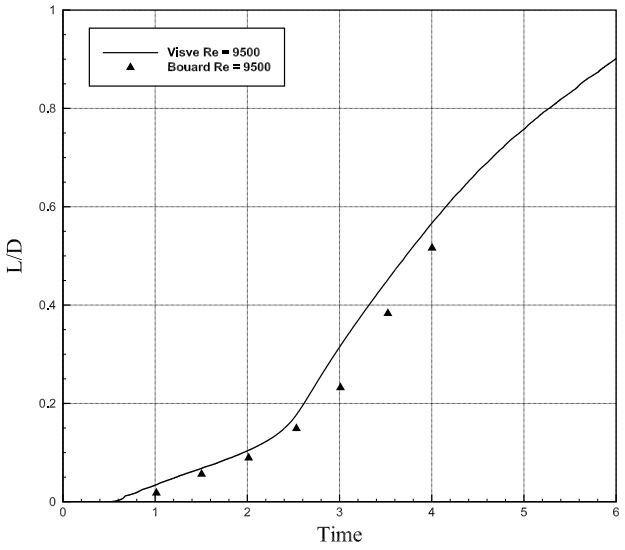

Figure 5.26: Time evolution of the wake length for $Re = 9500$ (experimental data of Bouard, 1980[4]).

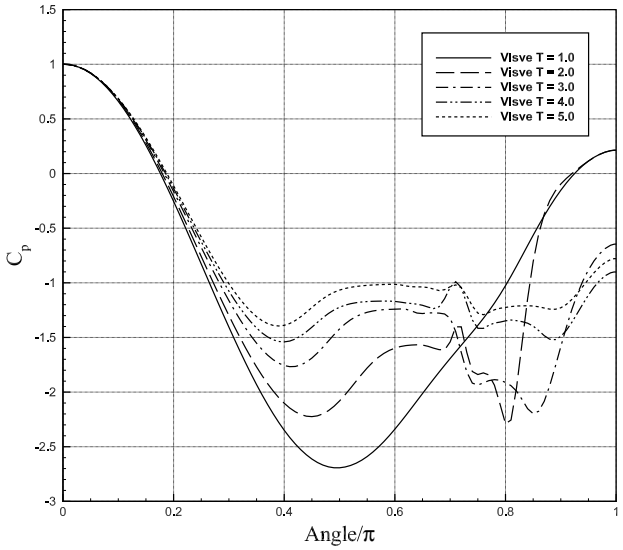

Figure 5.27: Time variation of the surface pressure coefficient for $Re = 9500$.

lished. We used 200×80 in Block I (200 panels on the cylinder and 80 cells in the radial direction) and 160 in Block II (extending 100 cells from the rear interface of Block I). The time step used this work is 0.0005. Reynolds number is 1000 in this case.

After a long time evolution, about $T > 120$, the vortex shedding process settles down, forming the regular vortex street pattern in the wake. The vorticities generated from the top and the bottom surface of the cylinder, periodically shedding in the wake region, and detached from the solid body. The detached vortices were flushed into the downstream, forming von Karman vortex street patterns. Figure 5.28 gives two snapshots of vorticity contours, which show vortices alternately shedding from the rear part of the cylinder. After the establishing of the stable vortex street pattern, periodic changes can

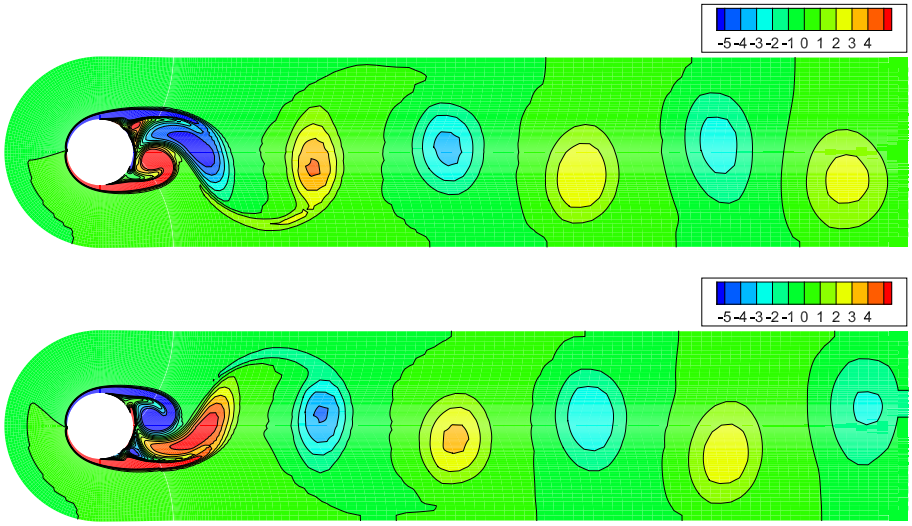

Figure 5.28: Long time results predicted by VISVE. Vorticity contours for $Re = 1000$ at $T = 146.0$ (upper) and $T = 154.0$ (lower).

Table 5.1: Average drag coefficient and Strouhal number at $Re = 1000$

	present	Fluent	Blackburn et al[3]	Qian et al [22]	Roshko [23]
C_d	1.55	1.39	1.51	1.52	1.20
S_t	0.264	0.22	-	0.240	0.21

be observed in the behavior of drag and lift coefficient.

A laminar case at $Re = 1000$ was run using Fluent 15.0 [1]. 100,000 meshes were used in the Fluent run, covering a domain of $40D \times 100D$. D is the diameter of the cylinder.

From the vortex shedding pattern, the Strouhal number $St = \frac{f \cdot D}{U}$ is about 0.264 and the average drag coefficient C_d is 1.55. As shown in Table 5.4, both results are in good agreement with published numerical data and

Table 5.2: Amplitude of unsteady C_d and C_l at $Re = 1000$

	present	Fluent (Laminar)	Qian et al[22]
C_d	0.13	0.13	0.23
C_l	1.19	1.17	1.41

experiment measurements. Both Strouhal number and average drag coefficient are slightly higher than the other data.

Figure 5.29 shows the C_d and C_l predicted by current method at $Re = 1000$. Comparing to Figure 5.29, the present method predicted somewhat higher average C_d. As shown in Table 5.4, the amplitudes of C_d and C_l are in good agreement with results from Fluent. We should note here, that a filter was applied to C_d and C_l predicted by our model. There were high frequency oscillations in the history of C_d and C_l, which were directly caused by the prediction of the surface pressure. As mentioned earlier in this thesis, the pressure solution has not converged yet at the current mesh resolution. This is an issue when integrating the surface pressure in order to get pressure drag on the cylinder.

In Figure 5.29, we can also see that at $T < 1.0$, C_d predicted by VISVE is huge. However in Qian and Vezza's work, they have a finite value (smaller than 1.0) at the beginning. This indicates that our pressure model may not be valid during the transition from potential flow to viscous flow.

In Figure 5.30, results predicted by the current VISVE model and Flu-

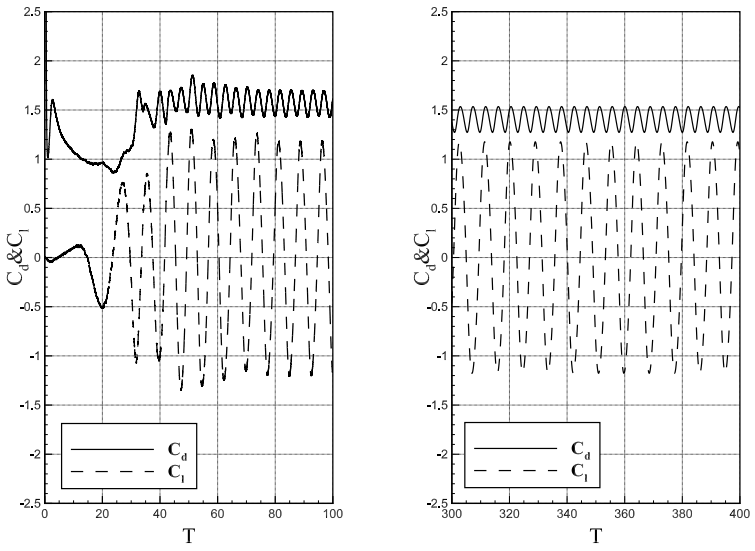

(a) (b)

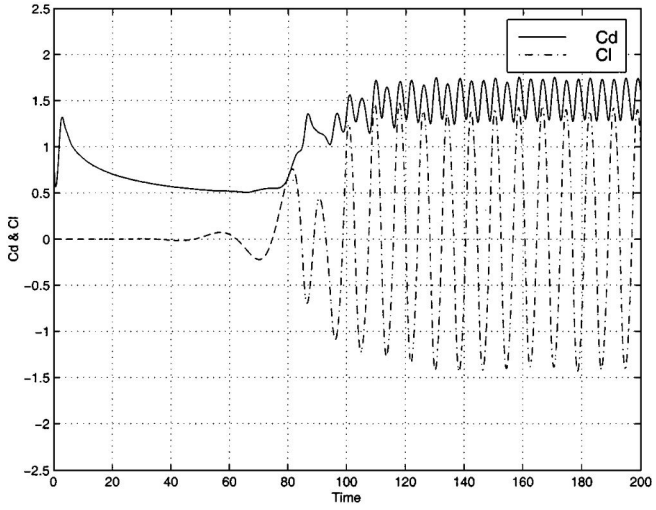

(c)

Figure 5.29: C_d and C_l predicted by current methods at $Re = 1000$, comparing with results from Fluent and numerical simulation from Qian and Vezza. (a) Predicted by current method at $Re = 1000$. (b) Predicted by Fluent using 100,000 meshes. (c) Numerical Simulation by Qian and Vezza (2001) [22].

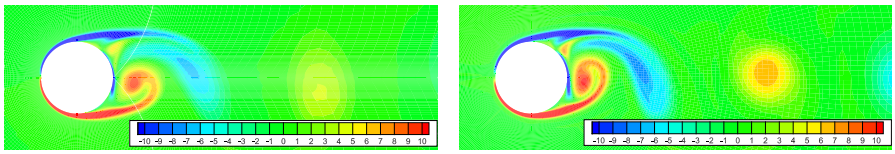

(a) VISVE $T = 131.0$ (b) Fluent $T = 296.3$

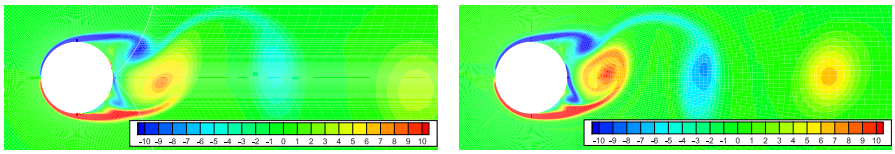

(c) VISVE $T = 132.0$ (d) Fluent $T = 297.3$

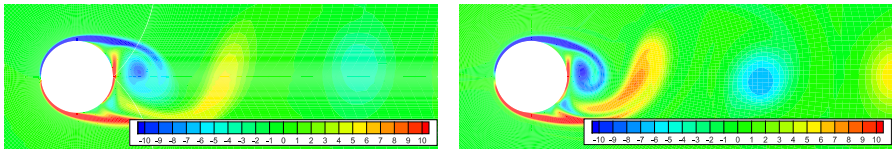

(e) VISVE $T = 133.0$ (f) Fluent $T = 298.3$

Figure 5.30: Vorticity contour predicted by VISVE and Fluent laminar model, with $\Delta t = 1$.

ent laminar flow model are compared. Since the Fluent case was not initiated using impulsively started flow, the results are compared at a later stage, after stable vortex patterns have been established. The flow patterns have small discrepancies. The over-diffusion observed in the VISVE results could be resolved with finer grid in the wake.

Chapter 6

Conclusions and Recommendations

6.1 Conclusions and Contributions

The main contributions of this thesis are:

1. Applied 2D Viscous Vorticity Equation (VISVE) solver to non-orthogonal mesh in order to simulate the flow around cylinder. New griding scheme was developed according to the cylinder flow geometry. The skewness of the grid was considered in the flow solver and the gradient of the vorticity was evaluated using the least squares method.

2. The flow field results are comparable to published experimental and numerical data. These various comparisons indicate that the simulation is sufficiently accurate and reliable. Therefore, this work quantitatively validates the 2D VISVE method.

3. A new method to predict the surface pressure was developed, in which only surface pressure were evaluated instead of calculating the pressure throughout the flow field. The new model provides comparable pressure and forces results to published data or results from other methods, as well as results from the commercial code ANSYS Fluent.

4. Taking advantage of the spatial concentration of the vorticity, the method uses much smaller computational domain than a N-S solver. The effect of grid resolution is carefully evaluated to ensure the convergence of the solution.

5. Improved computational efficiency by implementing parallel computing in the code.

6.2 Recommendations for Future Work

The original version of the VISVE model has been improved and validated for laminar flow in this thesis. However, the following improvements can be implemented in the future.

6.2.1 Pressure and Force Calculation

The solution of pressure at very early stage of the flow is vary inaccurate. The model of surface pressure is not valid for the very early stage of a potential inviscid flow. From potential flow to viscous flow, it may take some time for vorticity to diffuse to the whole fluid field, during which the gradient of vorticity at the solid surface might be off from the theoretical values. A correction may be included in the model in the early stage. Tests on the sensitivity of the solution with respect to the time step should be conducted in future works.

The noises of C_d and C_l profile are filtered in this thesis. C_d and C_l are

integrated from the surface pressure and shear stress. Viscous drag and lift are smooth during the time frame, but pressure drag and lift has noises, although at a certain time step, the pressure profile is smooth along the surface. More investigation needs to be done in finding the reason of the noises.

The integration model for pressure developed by Wu [31] is also practical. This model was tested in VISVE 2D model, but the pressure prediction has large discrepancy comparing with other numerical data, especially at angle larger than 0.6π. The C_d and C_l profiles predicted by this integration method also have the noises within the time frame. More works need to be done evaluating this integration model.

6.2.2 Effects of Turbulence

The current model includes only the laminar flow model. A turbulent model with a model of eddy viscosity could be developed in order to predict turbulent flow at high Reynolds number. Mixing length model[20] could be one of the simplest options, however there might be difficulties in:

1. Definition of the mixing length. Mixing length is an 1-D RANS model, thus to extend it in a 2-D or 3-D problem could be difficult. Close to the boundary within the boundary layer, mixing length could be defined as the distance to the wall, while outside of the boundary layer new model need to be determined for mixing length.

2. At the early stage of an impulsively start flow, the shear effect near the

solid surface may end up with large eddy viscosity if evaluated using mixing length model. Therefore, the physics of this process needs to be carefully designed when potential flow transforms into viscid flow with a sudden start.

Other than the simple mixing length model, a Large Eddy Simulation (LES) with Smagorinsky Model could be included in the subfilter scale(SFS) [20]. Mansfield et al (1998)[16] presented an application of a dynamic eddy diffusivity model within a viscous vorticity transport solver. More investigations need to be done in the eddy diffusivity model implemented near the boundary within our method.

6.2.3 Extension to alternating flow around cylinder

An alternating flow around the cylinder is also a challenging subject that could be simulated by current VISVE solver. Wang (2015) [28] and Li (2016) [15] simulated an oscillating flow around cylinder using commercial CFD software ANSYS Fluent. The VISVE solver can be applied to alternating flow around cylinder. The current griding scheme needs to be improved to resolve the wake on both sides of the cylinder.

When vortices are generated during the previous period, they will be convected back and hit the cylinder, and these vortices will travel upstream of the cylinder. Thus, investigation in the size of the computational domain should be conducted.

Bibliography

[1] ANSYS Inc. *ANSYS Inc. PDF Documentation for Release 15.0*, 15.0 edition, 2013.

[2] HM Badr and SCR Dennis. Time-dependent viscous flow past an impulsively started rotating and translating circular cylinder. *Journal of Fluid Mechanics*, 158:447–488, 1985.

[3] Hugh M Blackburn and Ron D Henderson. A study of two-dimensional flow past an oscillating cylinder. *Journal of Fluid Mechanics*, 385:255–286, 1999.

[4] Roger Bouard and Madeleine Coutanceau. The early stage of development of the wake behind an impulsively started cylinder for 40¡ re¡ 10 4. *Journal of Fluid Mechanics*, 101(03):583–607, 1980.

[5] Chien-Cheng Chang and Ruey-Ling Chern. A numerical study of flow around an impulsively started circular cylinder by a deterministic vortex method. *Journal of Fluid Mechanics*, 233:243–263, 1991.

[6] RR Clements. An inviscid model of two-dimensional vortex shedding. *Journal of Fluid Mechanics*, 57(02):321–336, 1973.

[7] Alexandre Dupuis, Philippe Chatelain, and Petros Koumoutsakos. An immersed boundary–lattice-boltzmann method for the simulation of the

flow past an impulsively started cylinder. *Journal of Computational Physics*, 227(9):4486–4498, 2008.

[8] Joseph P Giesing. Nonlinear two-dimensional unsteady potential flow with lift. *Journal of Aircraft*, 5(2):135–143, 1968.

[9] E Guilmineau and P Queutey. A numerical simulation of vortex shedding from an oscillating circular cylinder. *Journal of Fluids and Structures*, 16(6):773–794, 2002.

[10] Martin OL Hansen, Jens Nørkær Sørensen, and Wen Zhong Shen. Vorticity–velocity formulation of the 3d navier–stokes equations in cylindrical co-ordinates. *International journal for numerical methods in fluids*, 41(1):29–45, 2003.

[11] J Katz. A discrete vortex method for the non-steady separated flow over an airfoil. *Journal of Fluid Mechanics*, 102:315–328, 1981.

[12] Justin E Kerwin, Spyros A Kinnas, Jin-Tae Lee, and Wei-Zen Shih. A surface panel method for the hydrodynamic analysis of ducted propellers. *Trans. SNAME*, 95, 1987.

[13] Spyros A Kinnas and Ching-Yeh Hsin. The local error of a low-order boundary element method at the trailing edge of a hydrofoil and its effect on the global solution. *Computers & fluids*, 23(1):63–75, 1994.

[14] Petros Koumoutsakos and A Leonard. High-resolution simulations of the flow around an impulsively started cylinder using vortex methods. *Journal of Fluid Mechanics*, 296:1–38, 1995.

[15] Zhihao Li. Univerisity/navy/industry Consortium on Cavitation Performance of High Speed Propulsors, Ocean Engineerig Group, UT Austin. In *Volume of Forty-fifth Meeting*, pages 144–162, February 2016.

[16] John R Mansfield, Omar M Knio, and Charles Meneveau. A dynamic les scheme for the vorticity transport equation: Formulation anda prioritests. *Journal of Computational Physics*, 145(2):693–730, 1998.

[17] Sanjay Mittal and Bhaskar Kumar. Flow past a rotating cylinder. *Journal of Fluid Mechanics*, 476:303–334, 2003.

[18] Jayathi Y. Murthy. Numerical methods in heat, mass, and momentum transfer. 2002.

[19] XD Niu, YT Chew, and C Shu. Simulation of flows around an impulsively started circular cylinder by taylor series expansion-and least squares-based lattice boltzmann method. *Journal of Computational Physics*, 188(1):176–193, 2003.

[20] Stephen B Pope. *Turbulent flows*. Cambridge University Press, 2000.

[21] L Prandtl. The magnus effect and windpowered ships. *Naturwissenschaften*, 13:93–108, 1925.

[22] Ling Qian and M Vezza. A vorticity-based method for incompressible unsteady viscous flows. *Journal of Computational Physics*, 172(2):515–542, 2001.

[23] Anatol Roshko. On the development of turbulent wakes from vortex streets. 1954.

[24] Turgut Sarpkaya. An inviscid model of two-dimensional vortex shedding for transient and asymptotically steady separated flow over an inclined plate. *Journal of Fluid Mechanics*, 68(01):109–128, 1975.

[25] PR Spalart and Anthony Leonard. Computation of separated flows by a vortex-tracing algorithm. 1981.

[26] Ye Tian. *Leading Edge Vortex Modeling and its Effect on Propulsor Performance*. PhD thesis, Ocean Engineerig Group, UT Austin, The University of Texas at Austin, December 2014.

[27] Ye Tian and S.A. Kinnas. A numerical method for the analysis of unsteady cavitating rotor and stator interaction. In *Fourth International Symposium on Marine Propulsors*, 2015.

[28] Guangyao Wang. PIV Experiment and CFD Simulation of Flow around Cylinder. Master's thesis, Ocean Engineerig Group, UT Austin, The University of Texas at Austin, May 2015.

[29] Charles HK Williamson. Vortex dynamics in the cylinder wake. *Annual review of fluid mechanics*, 28(1):477–539, 1996.

[30] CHK Williamson and A Roshko. Vortex formation in the wake of an oscillating cylinder. *Journal of fluids and structures*, 2(4):355–381, 1988.

[31] Chunlin Wu. Univerisity/navy/industry Consortium on Cavitation Performance of High Speed Propulsors, Ocean Engineerig Group, UT Austin. In *Volume of Forty-fifth Meeting*, pages 82–99, February 2016.

[32] XH Wu, JZ Wu, and JM Wu. Effective vorticity-velocity formulations for three-dimensional incompressible viscous flows. *Journal of Computational Physics*, 122(1):68–82, 1995.